Available online at www.sciencedirect.com
SCIENCE DIRECT
International Journal of Mass Spectrometry 249–250 (2006) 263–278
International Journal of Mass Spectrometry
www.elsevier.com/locate/ijms

Gas-phase thermochemistry of the early cationic transition-metal sulfides of the second row: YS^+, ZrS^+, and NbS^+

Ilona Kretzschmar [a,*], Detlef Schröder [a], Helmut Schwarz [a], P.B. Armentrout [b,**]

[a] *Institut für Chemie der Technischen Universität Berlin, Straße des 17, Juni 135, D-10623 Berlin, Germany*
[b] *Department of Chemistry, University of Utah, Salt Lake City, UT 84112, USA*

Received 31 October 2005; received in revised form 12 December 2005; accepted 12 December 2005
Available online 20 January 2006

In memory of Chava Lifshitz, an inspiring friend, colleague, and mentor.

Abstract

The gas-phase reactivity of YS^+, ZrS^+, and NbS^+ towards oxygen-transferring reagents such as H_2O, CO, CO_2, and COS is investigated using guided-ion beam (GIB) and Fourier-transform ion cyclotron resonance (FTICR) mass spectrometry. A lower limit of $D_0(M^+–S) > 4.50 \pm 0.04$ eV for the sulfur binding energy is derived from the exothermic formation of MS^+ in the reaction of all three atomic metal ions, M^+, with CS_2. Upper limits for $D_0(M^+–S)$ are determined by collision-induced dissociation of MS^+ with Xe. The O-transfer experiments carried out in the GIB instrument lead to several estimates for $D_0(M^+–S)$, which are further refined by equilibrium constants K_{eq} derived from the reaction $MS^+ + H_2O \rightarrow MO^+ + H_2S$ and its reverse. Overall assessment of the results from ion–molecule reactions, collision-induced dissociation, and equilibrium measurements yields the 0 K bond energies of $D_0(Y^+–S) = 5.49 \pm 0.18$ eV, $D_0(Zr^+–S) = 5.69 \pm 0.10$ eV, $D_0(Nb^+–S) = 5.20 \pm 0.21$ eV, $D_0(Y^+–CS) = 1.42 \pm 0.08$ eV, $D_0(Zr^+–CS) = 2.67 \pm 0.11$ eV, and $D_0(Nb^+–CS) = 2.51 \pm 0.11$ eV, and heats of formation for $\Delta_f H_0(YOS^+) = 6.59 \pm 0.37$ eV, $\Delta_f H_0(ZrOS^+) = 8.45 \pm 0.33$ eV, $\Delta_f H_0(NbOS^+) = 9.05 \pm 0.27$ eV, $\Delta_f H_0(YS_2^+) = 6.96 \pm 0.70$ eV, and $\Delta_f H_0(ZrS_2^+) = 9.34 \pm 0.73$ eV.

Keywords: Yttrium sulfide; Zirconium sulfide; Niobium sulfide; Sulfur transfer; Transition-metal sulfide

1. Introduction

Transition-metal sulfides have wide utility in catalytic and electronic applications because of their high sulfur bond energies, their oxophilicity, as well as their intrinsic electronic and structural properties. Sulfidation of pure yttrium occurs at a rate of $\sim 6.5 \times 10^{-10}$ g^2 cm^4 s when exposed to a H_2/H_2S mixture ($P_{S_2} = 10^{-3}$ Pa) at 800 °C and leads to formation of visible scales on the yttrium surface. Analysis of the scales identifies them as consisting of Y_2O_2S because of the presence of oxygen-containing species in the H_2/H_2S mixture [1]. Y_2O_2S is a wide-gap semiconductor and is used in cathode ray tubes because it phosphoresces when doped with europium [2]. Mikami and Oshiyama [3,4] theoretically investigated Y_2O_2S in order to elucidate the electronic structure of a variety of intrinsic point defects found in this material. Control of the intrinsic defects for a variety of charge states is essential for the efficient exploitation of these semiconductor materials [4]. The electronic structure and infrared spectrum of ZrS_2 have been determined theoretically at the DFT/B3LYP level of theory and compared to experimental data from reaction of laser-ablated Zr with discharged sulfur atoms in an argon matrix [5]. Allali et al. [6] found differences in sulfurization of niobium precursors on different supports. The authors report that Nb precursors on a carbon support are easily sulfurized by flow of a N_2/H_2S (15%) mixture under atmospheric pressure at 400 °C for 4 h, whereas harsher treatment with CS_2 at 400 °C for 13 h is required for sulfurization of Nb in an alumina supported catalyst. NbS_2 is used as a hydrodesulfurization (HDS) and hydrodenitrogenation catalyst for hydrotreatment reactions in the purification of petroleum [7]. Further, it has been shown that

* Corresponding author. Present address: The City College of New York, Chemical Engineering Department, 140th Street at Convent Avenue, New York, NY 10031, USA. Tel.: +1 212 650 6769; fax: +1 212 650 6660.
** Corresponding author.
E-mail addresses: kretzschmar@ccny.cuny.edu (I. Kretzschmar), armentrout@chem.utah.edu (P.B. Armentrout).

1387-3806/$ – see front matter © 2006 Elsevier B.V. All rights reserved.
doi:10.1016/j.ijms.2005.12.017

doping of hydrotreated NiMo catalysts with 5 wt% niobium and activation with CS_2 affords Nb centers in a NbS_2 binding situation [8]. The HDS and hydrogenation (HYD) activity of such NiMoNb catalysts was found to be superior compared to plain NiMo catalysts. NbS_2 is also an effective humidity sensor [9]. Application of NbS_2 in cathode materials of secondary batteries is possible because of the layered structure of NbS_2, which facilitates intercalation into the van der Waals gap between these layers [10]. Further, $EuNb_2S_5$ synthesized by Istomin et al. [11] exhibits a superconducting phase at 3 K.

In the present study, we have investigated the interaction of sulfur with cations of the early metals of the second transition row, i.e., yttrium, zirconium, and niobium. The 0 K bond dissociation energies, $D_0(M^+–S)$, are derived using the guided-ion beam (GIB) and Fourier-transform ion cyclotron resonance (FTICR) mass spectrometric techniques. Quantum-chemical methods are employed to complement the thermodynamic data with information on electronic ground and low-lying excited states, bond lengths, and vibrational frequencies of MS^+ (M = Y–Nb).

2. Methods

GIB and FTICR mass spectrometry are used for the evaluation of thermodynamic data by means of threshold measurements of endothermic reactions and assessment of rate coefficients for exothermic processes, respectively. FTICR is also used to determine equilibrium constants in cases where neither activation barriers nor Gibbs free energies are too large.

2.1. GIB

Detailed descriptions of the guided-ion beam apparatus used in this study and the experimental procedures are given elsewhere [12,13]. Briefly, Ar^+ ions created in a dc discharge source [13] are accelerated towards a metal cathode thereby sputtering off M^+ ions (M = Y, Zr, and Nb). The metal ions drift in a meter-long flow tube operated with a 9:1 mixture of helium and argon at a pressure of ~90 Pa. The ions undergo ~10^5 collisions with the buffer gas before exiting the flow tube, and therefore are expected to equilibrate to room temperature [14]. Because helium and argon do not always effectively quench excited states of atomic transition-metal ions [15], methane is introduced ca. 25 cm downstream from the discharge at pressures between 0.07 and 0.8 Pa. Operation at these pressures allows the ions to undergo 10^2–10^3 collisions with methane in the flow tube, which is sufficient to remove virtually all excited states of the metal ions under study [16].

MX^+ ions (X = O and S) are generated by addition of O_2 and COS, respectively, to the flow 75 cm downstream from the source. Given the limited mass resolution of the GIB experiment, YS^+ with a mass of $m/z = 121$ is very close to $(COS)_2^+$ ($m/z = 120$) which is produced in large abundance at high COS pressures. Optimization of the COS pressure and mass selection lead to a reasonable intensity for the YS^+ beam; under these conditions, the cross-section of the COS^+ fragment indicative of $(COS)_2^+$ is smaller than 0.02×10^{-16} cm^2 upon CID with Xe. The m/z ratio of the YO^+ species is also recorded to probe contributions of isobaric YO_2^+ ions to the YS^+ beam. The cross-section obtained at $m/z = 105$ (YO^+) is below the detection limit of the instrument (0.01×10^{-16} cm^2) and thus it is concluded that the amount of YO_2^+ in the beam is negligible if present at all. For M = Zr and Nb, no MO^+ signal was detected in the preliminary mass scan.

Following extraction from the source, the ions are accelerated and focused into a magnetic sector, mass-selected, decelerated to a desired kinetic energy, and focused into an octopole ion trap [12]. This device guides the ions through a static gas cell kept at a low pressure (~0.007–0.013 Pa) of the reactant gas. It was verified that all product cross-sections reported result from single ion–molecule collisions by examining the pressure dependence of the product intensities. After exiting the gas cell, product and unreacted beam ions drift to the end of the octopole where they are directed into a quadrupole mass filter for mass analysis and then detected. Conversion of the raw ion intensities into reaction cross-sections and the calibration of the absolute energy scale are treated as described previously [12]. The accuracy of the absolute cross-sections is estimated to be ±20%. The beams have Gaussian kinetic energy distributions with average full widths at half maximum (FWHM) of ca. 0.25 eV in the laboratory frame. The uncertainty of the absolute energy scale is ±0.05 eV (laboratory).

Quantitative analysis of the energy dependence of these cross-sections is achieved using Eq. (1) and methods outlined elsewhere [17].

$$\sigma(E) = \sigma_0 \sum \frac{g_i(E + E_i - E_0)^n}{E} \quad (1)$$

In Eq. (1), E is the relative kinetic energy of the reactants, E_0 the threshold for reaction at 0 K, σ_0 a scaling parameter, and n is a fitting parameter. The summation is over the rovibrational states of the reactants having energies E_i and populations g_i ($\sum g_i = 1$). Before comparison with the data, this equation is convoluted over the translational energy distributions of both reactants. This determination of the reaction thresholds involves explicit consideration of the distributions of vibrational, rotational, and translational energies of both reactants. Because all sources of reactant energy are considered, the thermochemistry obtained corresponds to 0 K values in all cases.

2.2. FTICR

A Spectrospin CMS-47X FTICR mass spectrometer with an external ion source [18] is used to investigate the reactions of the transition-metal sulfide and oxide cations (MS^+ and MO^+) with H_2O and H_2S, respectively. M^+ ions are generated via laser desorption/laser ionization by focusing the beam of a Nd:YAG laser (Spectron Systems, λ = 1064 nm) onto a metal target. The ions are extracted from the source and transferred into the analyzer cell by a system of electrostatic potentials and lenses. After deceleration, the ions are trapped in the field of a superconducting magnet (maximum field strength 7.05 T). The most abundant isotope (^{89}Y, ^{90}Zr, and ^{93}Nb, respectively) is mass-selected using front-end resolution enhancement with tailored

sweeps (FERETS) [19], a computer assisted protocol that combines frequency sweeps and single frequency ion-ejection pulses to optimize ion isolation. Generation of the MO^+ and MS^+ ions is achieved by reaction of M^+ with pulsed-in O_2 and COS, respectively. For the purpose of thermalization, the ions are collided with pulsed-in methane (maximum pressure ca. 4×10^{-3} Pa, ca. 2000 collisions) prior to reaction. The kinetics of all reactions are carefully studied as a function of thermalizing collisions in order to ensure that the ions undergoing subsequent ion–molecule reactions are not kinetically and/or electronically excited. The reactants are admitted to the cell via leak valves at stationary pressures between 1 and 13×10^{-6} Pa (as measured by a Balzers IMG070 ion gauge). The first-order kinetics of the reacting ions provide the rate constants k_{exp}, determined by linear regression, which are compared to the gas-kinetic collision rates [20], k_c, and expressed in terms of reaction efficiencies, $\phi = k_{exp}/k_c$.

2.3. Calculations

The bond lengths and the ground state/excited state splittings of MS^+ (M = Y, Zr, and Nb) are calculated with density functional theory (DFT). The DFT calculations are carried out using the Amsterdam density functional (ADF, Version 2.0.1) suite of programs [21] with the inner-shell electrons ([Ne] for S and [Ar] for M) treated in the frozen-core approximation [22]. The valence orbitals are expanded as linear combinations of Slater-type basis functions. Triple-zeta basis sets are used for yttrium, zirconium, niobium, and sulfur. All molecular and atomic energies are calculated using the local spin density approximation (LDA) with Slater's exchange functional and the Vosko–Wilk–Nusair parametrization (VWN) [23] augmented by Becke's [24] and Perdew's [25] (BP) gradient corrections for the exchange and correlation potentials, respectively [26]. This method will be referred to as ADF/BP. Particular advantages of the ADF program are that it provides control over the symmetry of the wave function created during geometry optimizations and permits the calculations of the excited states.

3. Experimental results

In the following, mass spectrometric data from two complementary instruments are presented to explore the gas-phase reactivity of YS^+, ZrS^+, and NbS^+. First, the two exothermic reactions of M^+ (M = Y, Zr, and Nb) with COS and CS_2 are studied followed by collision-induced dissociation of MS^+ (M = Y, Zr, and Nb) with Xe. Next, the reaction of MS^+ (M = Y, Zr, and Nb) with the oxygen compounds CO, CO_2, and COS as well as MO^+ with CS_2 are analyzed, further refining the thermochemistry of MS^+. Finally, results from indirect equilibrium measurements of reaction (2) and its reverse (2′) in the FTICR are presented as an independent means for determination of $D_0(M^+–S)$.

$$MS^+ + H_2O \rightleftarrows MO^+ + H_2S \quad (2)$$

The thermochemical data used in this study are summarized in Tables 1 and 2.

Table 1
Heats of formation and bond dissociation energies for ionic species at 0 K

Ionic species	$\Delta_f H^\circ$ [eV][a]	Bond	D_0 [eV]
Y^+	10.58 (0.05)[b]		
Zr^+	13.16 (0.26)[c]		
Nb^+	14.45 (0.08)[c]		
YC^+	15.04 (0.13)	Y^+—C	2.91 ± 0.12[d]
ZrC^+	15.81 (0.28)	Zr^+—C	4.72 ± 0.11[d]
NbC^+	16.66 (0.17)	Nb^+—C	5.16 ± 0.15[d]
YO^+	5.86 (0.19)	Y^+—O	7.28 ± 0.18[d]
ZrO^+	7.96 (0.28)	Zr^+—O	7.76 ± 0.11[d]
NbO^+	9.88 (0.14)	Nb^+—O	7.13 ± 0.11[d]
YS^+	7.93 (0.19)	Y^+—S	5.49 ± 0.18[e]
ZrS^+	10.31 (0.28)	Zr^+—S	5.69 ± 0.10[e]
NbS^+	12.10 (0.22)	Nb^+—S	5.20 ± 0.21[e]
YCO^+	9.09 (0.12)	Y^+—CO	0.31 ± 0.11[f]
$ZrCO^+$	11.18 (0.28)	Zr^+—CO	0.80 ± 0.10[g]
$NbCO^+$	12.28 (0.09)	Nb^+—CO	0.99 ± 0.05[h]
YCS^+	12.01 (0.10)	Y^+—CS	1.42 ± 0.08[e]
$ZrCS^+$	13.34 (0.29)	Zr^+—CS	2.67 ± 0.11[e]
$NbCS^+$	14.79 (0.14)	Nb^+—CS	2.51 ± 0.11[e]
YO_2^+	6.66 (0.25)	OY^+—O	1.76 ± 0.16[i]
ZrO_2^+	6.67 (0.29)	OZr^+—O	3.85 ± 0.07[g]
NbO_2^+	6.73 (0.22)	ONb^+—O	5.71 ± 0.17[h]
YOS^+	6.59 (0.37)	SY^+—O	3.93 ± 0.32[e]
		OY^+—S	2.14 ± 0.42[e]
$ZrOS^+$	8.45 (0.33)	SZr^+—O	4.42 ± 0.18[e]
		OZr^+—S	2.36 ± 0.44[e]
$NbOS^+$	9.05 (0.27)	SNb^+—O	5.61 ± 0.16[e]
		ONb^+—S	3.68 ± 0.31[e]
YS_2^+	6.96 (0.70)	SY^+—S	3.82 ± 0.68[e]
ZrS_2^+	9.34 (0.73)	SZr^+—S	3.82 ± 0.68[e]
NbS_2^+	<10.45 (0.23)	SNb^+—S	>4.50 ± 0.04e

[a] If not stated otherwise, these values are calculated from the corresponding thermochemical data given in Tables 1 and 2.
[b] Ref. [52].
[c] Ref. [53].
[d] Ref. [33].
[e] This work.
[f] Ref. [54].
[g] Ref. [55].
[h] Ref. [56].
[i] Ref. [57].

3.1. Reaction of M^+ with COS

The reaction of M^+ with COS is studied with FTICR only. The primary products observed are MS^+ and MO^+ (reactions (3) and (4)). MS_2^+ (M = Y, Zr, and Nb) is also observed as a secondary product formed at longer reaction times. For zirconium, formation of $ZrOS^+$ is observed at long reaction times, which is attributed to reactions with impurities such as O_2 or H_2O.

$$M^+ + COS \rightarrow MS^+ + CO \quad (3)$$

$$M^+ + COS \rightarrow MO^+ + CS \quad (4)$$

The measured rate constants k_{exp} for MS^+ formation (reaction (3)) are $(4.3 \pm 0.8) \times 10^{-10}$, $(5.2 \pm 1.0) \times 10^{-10}$, and $(4.7 \pm 0.69) \times 10^{-10}$ cm^3 s^{-1} molecule^{-1} for M = Y, Zr, and Nb, respectively. The rates are corrected for MO^+ formation amounting to 25, 45, and 15% for M = Y, Zr, and Nb, respectively.

Table 2
Heats of formation and bond dissociation energies for neutral species at 0 K[a]

Neutral species	$\Delta_f H^\circ$ [eV]	Bond	D_0 [eV]
C	7.371 (0.005)		
S	2.847 (0.003)		
O	2.558 (0.001)	O—O	5.116 (0.001)
CO	−1.180 (0.002)	C—O	11.109 (0.005)
CS	2.85 (0.04)[b]	C—S	7.37 (0.04)
SO	0.052 (0.013)	S—O	5.353 (0.013)
S_2	1.330 (0.003)	S—S	4.364 (0.005)
CS_2	1.200 (0.008)[c]	SC—S	4.50 (0.04)
COS	−1.473 (0.003)[c]	OC—S	3.140 (0.005)
		SC—O	6.88 (0.04)
CO_2	−4.075 (0.001)	OC—O	5.453 (0.002)
SO_2	−3.075 (0.004)	OS—O	5.974 (0.014)
		S—O_2	5.922 (0.005)
H_2O	−2.476 (0.001)	H_2—O	5.034 (0.001)
H_2S	−0.182 (0.008)	H_2—S	3.029 (0.009)

[a] Footnote 'c' from Table 1 unless noted otherwise.
[b] Ref. [58].
[c] Ref. [59]. Corrected to 0 K using the H°–H° (298.15 K) values taken from the reference given in footnote 'b' of Table 1.

Efficiencies, $\phi(MS^+)$, as defined above, amount to 0.38 ± 0.07, 0.46 ± 0.08, and 0.36 ± 0.06 for reaction of COS with Y^+, Zr^+, and Nb^+, respectively. Comparison to $\phi(MS^+)$ with M = Sc, Ti, and V of 0.35 ± 0.07, 0.37 ± 0.07, and 0.21 ± 0.04, respectively [27], reveals that the second-row transition-metal cations exceed their lower congeners in reactivity. Assignment of the MO^+ product to reaction (4) is somewhat ambiguous because the early transition-metals cations are very reactive towards background contaminants such as water and oxygen. Further, MO^+ may also form as a secondary product upon reaction of MS^+ with the background contaminants. Careful examination of the FTICR data reveals that MO^+ forms as a primary product for all three metals. The rate constants k_{exp} for MO^+ formation (reaction (4)) are determined as $(1.4 \pm 0.3) \times 10^{-10}$, $(4.2 \pm 0.8) \times 10^{-10}$, and $(0.06 \pm 0.03) \times 10^{-10}$ $cm^3\ s^{-1}$ $molecule^{-1}$ for M = Y, Zr, and Nb, respectively. The exothermicity of reactions (3) and (4) indicates lower limits of $D_0(M^+–S) > 3.140 \pm 0.005$ eV and $D_0(M^+–O) > 6.88 \pm 0.04$ eV for M = Y, Zr, and Nb, respectively (Tables 1 and 2). The latter limits for $D_0(M^+–O)$ agree with known thermochemistry (Table 1).

3.2. Reaction of M^+ with CS_2

The reaction of M^+ with CS_2 is measured using the GIB and yields two major products, MS^+ and MCS^+, and as a minor product, MC^+, as shown in reactions (5)–(7). Product cross-sections are depicted in Fig. 1. $CS_2{}^+$ is seen as a minor product for M = Nb with an endothermic cross-section smaller than 0.05×10^{-16} cm^2 at high energies (not shown). Formation of $MS_2{}^+$ is observed for all three metals, but pressure dependence studies reveal that it results from multiple collisions with CS_2. Minor amounts of YO^+ ($\sigma_0 < 0.02 \times 10^{-16}$ cm^2) were also observed and attributed to reaction with residual water and oxygen in the reaction chamber (not shown).

$$M^+ + CS_2 \rightarrow MS^+ + CS \quad (5)$$

$$M^+ + CS_2 \rightarrow MCS^+ + S \quad (6)$$

$$M^+ + CS_2 \rightarrow MC^+ + S_2 \quad (7)$$

As can be seen from Fig. 1, Y^+, Zr^+, and Nb^+ react exothermically with CS_2 raising the lower limit to $D_0(M^+–S) > 4.50 \pm 0.04$ eV for M = Y, Zr, and Nb.

The MS^+ (M = Y, Zr, and Nb) cross-sections exhibit E^{-p} energy dependences with $p = 0.32 \pm 0.04$, 0.36 ± 0.02, and 0.29 ± 0.08, respectively, in the low-energy region (0.02–0.3 eV), changing to $p = 0.88 \pm 0.12$, 1.08 ± 0.20, and 1.14 ± 0.08 at energies above 0.3 eV. Below 0.02 eV the YS^+ and ZrS^+ cross-sections appear to converge to the LGS model (σ_{LGS}, dashed lines in Fig. 1). Above ca. 4.5 eV, all three MS^+ cross-sections decline more rapidly, probably because of the dissociation of the products (process (8)), which starts at 4.50 ± 0.04 eV (Table 2).

$$M^+ + CS_2 \rightarrow MS^+ + CS \rightarrow M^+ + CS + S \quad (8)$$

The energy dependences of ca. $E^{-0.3}$ at low interaction energies are in contrast to the LGS model, which predicts an $E^{-0.5}$ behavior [28]. Similar deviations from σ_{LGS} have been observed, for example, by Schultz and Armentrout in the charge-transfer (CT) reactions of $N_4{}^+$ with Kr and Xe and $N_2{}^+$ with H_2 [13,29]. For the $N_2{}^+/H_2$ system one explanation put forward is that the occurrence of charge transfer in the entrance channel allows the magnitude of the cross-section to be controlled by the polarizability of N_2, which is larger than that of H_2 [29]. In addition, Tosi et al. [30] developed a model for quasi-resonant charge-transfer processes, which predicts an $E^{-1/3}$ dependence for CT cross-sections. However, these arguments cannot explain the deviations from σ_{LGS} observed in this study, because process (5) is unlikely to involve CT at low energies considering the large difference between the ionization energies of CS_2 (IE = 10.0685 ± 0.0020 eV) [31] and the metal cations (IE < 6.83 eV) [32]. Sievers et al. [33] also observed deviations from σ_{LGS} for the exothermic formation of MO^+ in the M^+/O_2 systems (M = Y, Zr, and Nb). Their model of explanation involves the influence of the strongly attractive Coulombic potential of the $M^{2+} + O_2{}^-$ asymptote at low energies, which allows the reactants with large impact parameters to react at increased energies by crossing from the ion-induced dipole potential to the Coulombic potential. However, Sievers et al. find this model to be only in qualitative, but not in quantitative agreement with the experimental conditions, which led to their conclusion that potential–energy curves evolving from excited states of M^+ may also contribute.

Experimental artifacts caused by the uncertainty in the center-of-mass energy in the low-energy region can also be excluded as origin of the observed $E^{-0.3}$ dependence. For energies significantly below one FWHM of the beam spread (here about 0.09 ± 0.03 eV CM; see error ranges in Fig. 1a and b), the assumption that the ion-energy distribution can be represented by a truncated Gaussian becomes questionable. This can lead to

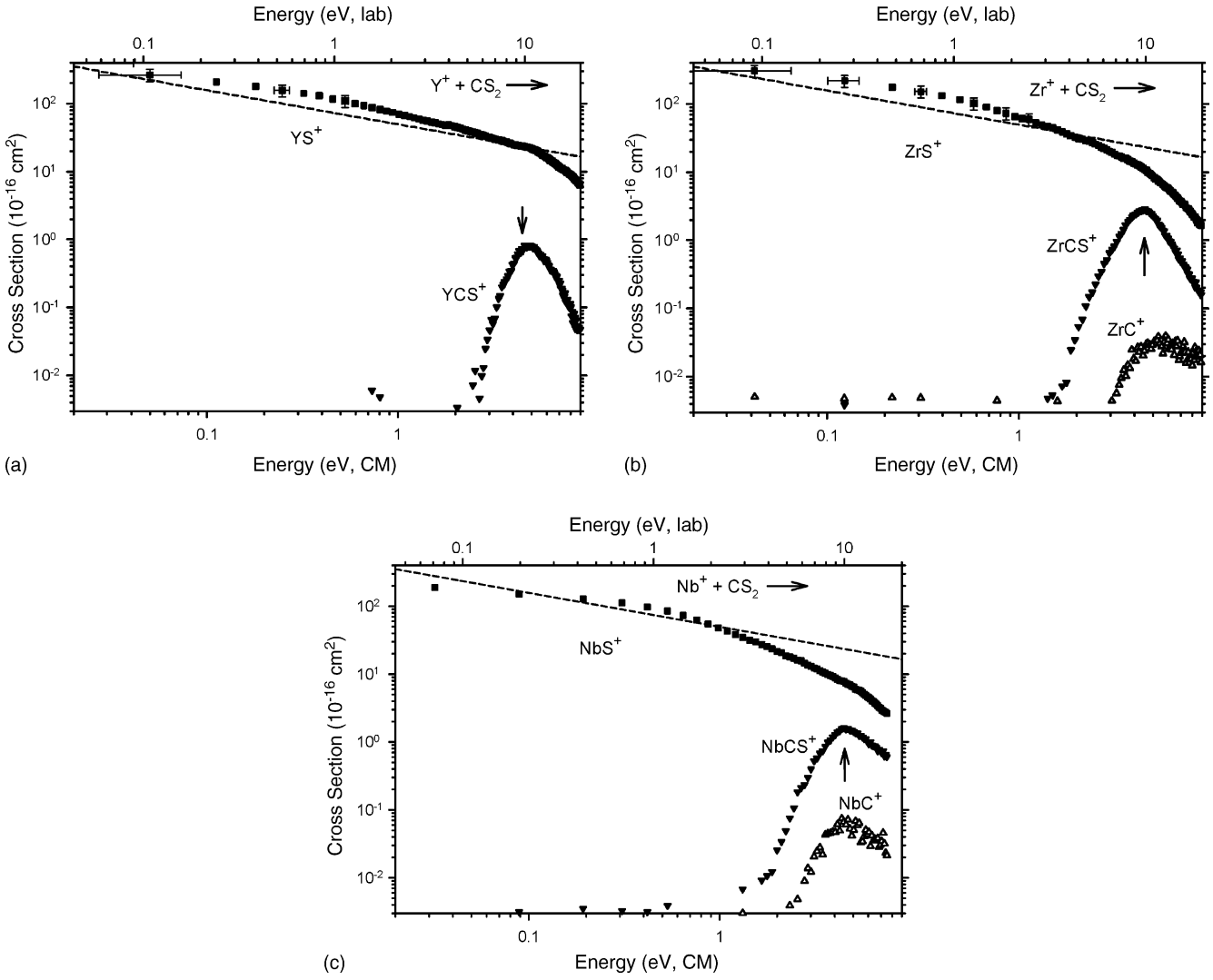

Fig. 1. Product cross-sections for the reaction M^+ ((a) Y^+; (b) Zr^+; (c) Nb^+) with CS_2 to form MS^+ (■), MCS^+ (▼), and MC^+ (△) as function of center of mass energy (lower axis) and laboratory energy (upper axis). The arrow marks D_0(S–CS) = 4.50 eV. The dashed lines represent σ_{LGS}. Error bars derived from beam spread (here about 0.09 ± 0.03 eV CM).

calculated average energies that are smaller than the true average energies produced in the laboratory. The net result of this process is that the cross-sections calculated at the lowest energies are shifted to lower energies by a small amount, such that the apparent cross-section begins to level off [34].

In order to obtain more information about reaction (5), M^+ ions (M = Y, Zr, and Nb) are reacted with CS_2 in the FTICR. MS^+ is formed as a primary product for all three metals. MO^+ is detected for M = Y and Nb and can be attributed to reaction with residual water and O_2 in the reaction cell (see below). MS_2^+ is only formed as a secondary product in the Nb^+/CS_2 system implying a lower limit of $D_0(SNb^+–S) > 4.50 \pm 0.04$ eV and an upper limit of $D_0(SM^+–S) < 4.50 \pm 0.04$ eV for M = Y and Zr. Reaction rates for MS^+ formation (reaction (5)) amount to $k_{FTICR} = (10.58 \pm 0.33) \times 10^{-10}$, $(9.14 \pm 2.11) \times 10^{-10}$, and $(8.15 \pm 0.82) \times 10^{-10}$ cm^3 s^{-1} molecule^{-1} for M = Y, Zr, and Nb, respectively. Reaction rates have been corrected for 25 and 5% MO^+ formation for M = Y and Nb, respectively. In comparison, the phenomenological rate constant k_{GIB} derived from the GIB cross-sections [35] at the lowest energies measured are $(11.5 \pm 5.8) \times 10^{-10}$, $(11.0 \pm 5.5) \times 10^{-10}$, and $(7.0 \pm 3.5) \times 10^{-10}$ cm^3 s^{-1} molecule^{-1} for M = Y, Zr, and Nb, respectively. Thus, the rate constants from both measurements are in good agreement confirming the observed $E^{-0.3}$ dependence. Interestingly, the deviation from σ_{LGS} in the M^+/O_2 and M^+/CS_2 systems is only observed in reactions of metal cations from the second transition row, but not for the Sc^+, Ti^+, and V^+ congeners [27]. This observation might point to the fact that the deviation is a result of the higher masses and larger radii of the second transition-row metal cations involved. For a more detailed discussion of this argument, see ref. [36].

The formation of the metal-thiocarbonyls (reaction (6)) is endothermic for all three metals (Fig. 1). Analysis of the MCS^+ cross-sections using Eq. (1) yields thresholds for YCS^+, $ZrCS^+$, and $NbCS^+$ (Tables 3–5) that are converted to $D_0(Y^+–CS) = 1.42 \pm 0.08$ eV, $D_0(Zr^+–CS) = 2.67 \pm 0.11$ eV, and $D_0(Nb^+–CS) = 2.51 \pm 0.11$ eV. These values are likely to represent lower limits because of competition with the very effi-

Table 3
Summary of parameters in Eq. (1) used for fitting the cross-sections and the derived $D_0(Y^+–S)$ in eV

Reaction		E_0 (eV)[a]	σ_0 (10^{-16} cm^2)	n	$D_0(Y^+–S)$ (eV)
$CS_2 + Y^+ \rightarrow YS^+ + CS$	(5)	<0	346[b]		>4.50 (0.04)
$CS_2 + Y^+ \rightarrow YCS^+ + S$	(6)	3.08 (0.02)	0.35 (0.01)	1.5 (0.2)	
$Xe + YS^+ \rightarrow Y^+ + S + Xe$	(10)	6.35 (0.18)	1.02 (0.30)	1.8 (0.1)	<6.35 (0.18)
$CO + YS^+ \rightarrow Y^+ + COS$	(11)	2.38 (0.17)	0.02 (0.01)	1.8 (0.2)	5.52 (0.17)
$CO + YS^+ \rightarrow YO^+ + CS$	(12)	3.02 (0.21)	0.14 (0.06)	1.6 (0.2)	6.56 (0.28)
$CO + YS^+ \rightarrow Y^+ + S + CO$	(13) [c]	7.14 (0.14)	0.33 (0.08)	0.7 (0.2)	<7.14 (0.14)
$CO + YS^+ \rightarrow YSO^+ + C$	(14)	6.97 (0.22)	0.02 (0.01)	1.7 (0.2)	
$CO_2 + YS^+ \rightarrow YO^+ + COS$	(16) [c]	1.03 (0.11)	0.73 (0.17)	1.7 (0.2)	6.00 (0.21)
$CO_2 + YS^+ \rightarrow YSO^+ + CO$	(17)	1.77 (0.24)	0.03 (0.01)	1.9 (0.2)	
$CO_2 + YS^+ \rightarrow Y^+ + S + CO_2$	(19)	6.43 (0.23)	0.37 (0.16)	1.4 (0.5)	<6.43 (0.23)
$COS + YS^+ \rightarrow YS_2^+ + CO$	(24)	<0	1[b]		
(26)$COS + YS^+ \rightarrow Y^+ + S_2 + CO$		4.37 (0.13)	0.26 (0.05)	2.0 (0.2)	5.59 (0.13)

[a] The E_0 values are the average of several threshold fits with uncertainties of one standard deviation.
[b] Maximum cross-section at $E_{CM} \approx 0.03$ eV.
[c] Fitting parameters for the endothermic feature after subtraction of the low energy part (see text).

Table 4
Summary of parameters in Eq. (1) used for fitting the cross-sections and the derived $D_0(Zr^+–S)$ in eV

Reaction		E_0 (eV)[a]	σ_0 (10^{-16} cm^2)	n	$D_0(Zr^+–S)$ (eV)
$CS_2 + Zr^+ \rightarrow ZrS^+ + CS$	(5)	<0	383[b]		>4.50 (0.04)
$CS_2 + Zr^+ \rightarrow ZrCS^+ + S$	(6)	1.83 (0.05)	1.03 (0.19)	2.7 (0.1)	
$CS_2 + Zr^+ \rightarrow ZrC^+ + S_2$	(7)	2.95 (0.14)	0.07 (0.01)	1.2 (0.2)	
$Xe + ZrS^+ \rightarrow Zr^+ + S + Xe$	(10)	6.72 (0.22)	1.25 (0.52)	1.6 (0.2)	<6.72 (0.22)
$CO + ZrS^+ \rightarrow Zr^+ + COS$	(11) [c]	2.72 (0.25)	0.03 (0.01)	1.8 (0.2)	5.86 (0.25)
$CO + ZrS^+ \rightarrow ZrO^+ + CS$	(12)	2.55 (0.24)	0.35 (0.14)	1.8 (0.2)	6.57 (0.27)
$CO + ZrS^+ \rightarrow Zr^+ + S + CO$	(13) [d]	6.93 (0.33)	1.29 (0.69)	1.6 (0.2)	<6.93 (0.33)
$CO + ZrS^+ \rightarrow ZrSO^+ + C$	(14)	6.43 (0.24)	0.92 (0.51)	1.9 (0.3)	
$CO_2 + ZrS^+ \rightarrow ZrO^+ + COS$	(16)	1.34 (0.37)	0.41 (0.24)	1.9 (0.1)	6.79 (0.39)
$CO_2 + ZrS^+ \rightarrow ZrSO^+ + CO$	(17) [d]	1.07 (0.10)	0.53 (0.25)	1.4 (0.2)	
$CO_2 + ZrS^+ \rightarrow Zr^+ + S + CO_2$	(19)	6.68 (0.22)	0.36 (0.12)	1.8 (0.1)	<6.68 (0.22)
$COS + ZrS^+ \rightarrow ZrS_2^+ + CO$	(24)	<0	188[b]		
$COS + ZrS^+ \rightarrow ZrO^+ + CS_2$	(25)	1.34 (0.21)	0.06 (0.02)	1.6 (0.2)	6.72 (0.24)
$COS + ZrS^+ \rightarrow Zr^+ + S_2 + CO$	(26)	5.25 (0.16)	0.28 (0.07)	2.0 (0.1)	6.47 (0.13)
$COS + ZrS^+ \rightarrow ZrO^+ + CS + S$	(27) [d]	5.65 (0.34)	1.37 (0.36)	1.1 (0.1)	6.53 (0.36)
$CS_2 + ZrO^+ \rightarrow ZrS_2^+ + CO$	(28)	<0	10[b]		
$CS_2 + ZrO^+ \rightarrow ZrS^+ + COS$	(29)	<0	0.3[b]		>5.38 (0.12)
$CS_2 + ZrO^+ \rightarrow ZrOS^+ + CS$	(30)	1.19 (0.13)	1.28 (0.27)	1.2 (0.2)	

[a] The E_0 values are the average of several threshold fits with uncertainties of one standard deviation.
[b] Maximum cross-section at $E_{CM} \approx 0.03$ eV.
[c] Low-energy, endothermic feature is reproduced with given parameters but the parameter n is held constant.
[d] Fitting parameters for the endothermic feature after subtraction of the low energy part (see text).

Table 5
Summary of parameters in Eq. (1) used for fitting the cross-sections and the derived $D_0(Nb^+–SNb^+–S)$ in eV

Reaction		E_0 (eV)[a]	σ_0 (10^{-16} cm^2)	n	$D_0(Nb^+–S)$ (eV)
$CS_2 + Nb^+ \rightarrow NbS^+ + CS$	(5)	<0	195[b]		>4.50 (0.04)
$CS_2 + Nb^+ \rightarrow NbCS^+ + S$	(6)	1.99 (0.05)	1.01 (0.15)	2.2 (0.1)	
$CS_2 + Nb^+ \rightarrow NbC^+ + S_2$	(7)	2.59 (0.30)	0.08 (0.09)	1.5 (0.5)	
$Xe + NbS^+ \rightarrow Nb^+ + S + Xe$	(10)	6.09 (0.16)	1.11 (0.36)	1.9 (0.2)	<6.09 (0.16)
$CO + NbS^+ \rightarrow NbO^+ + CS$	(12)	2.58 (0.42)	0.09 (0.09)	2.2 (0.2)	5.97 (0.43)
$CO + NbS^+ \rightarrow Nb^+ + S + CO$	(13)	6.09 (0.26)	1.61 (0.66)	1.6 (0.2)	<6.09 (0.26)
$CO + NbS^+ \rightarrow NbSO^+ + C$	(14)	5.55 (0.21)	0.50 (0.19)	1.7 (0.2)	
$CO_2 + NbS^+ \rightarrow NbSO^+ + CO$	(17)	<0	53[b]		
$CO_2 + NbS^+ \rightarrow NbO^+ + CO + S$	(18)	3.71 (0.19)	2.47 (1.72)	1.2 (0.2)	5.39 (0.22)
$CO_2 + NbS^+ \rightarrow Nb^+ + S + CO_2$	(19)	6.44 (0.29)	0.85 (0.38)	1.6 (0.2)	<6.44 (0.29)
$COS + NbS^+ \rightarrow NbS_2^+ + CO$	(24)	<0	69[b]		
$COS + NbS^+ \rightarrow Nb^+ + S_2 + CO$	(26)	4.74 (0.33)	0.37 (0.22)	2.0 (0.2)	5.96 (0.33)
$COS + NbS^+ \rightarrow NbO^+ + CS + S$	(27)	5.18 (0.52)	0.44 (0.30)	1.5 (0.2)	5.43 (0.53)

[a] The E_0 values are the average of several threshold fits with uncertainties of one standard deviation.
[b] Maximum cross-section at $E_{CM} \approx 0.03$ eV.

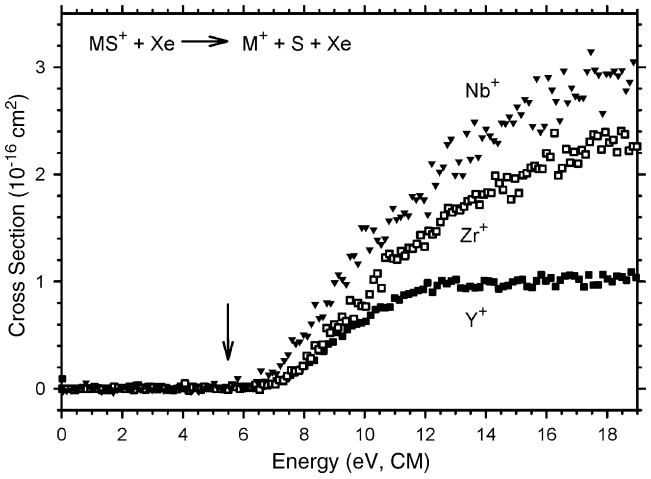

Fig. 2. Product cross-sections for the CID process of MS^+, YS^+ (■), ZrS^+ (□), and NbS^+ (▼), with xenon as a function of center of mass energy. The arrow marks the approximate M^+–S bond energies at 5.5 eV.

cient reaction (5). All three MCS^+ cross-sections fall off sharply above 4.5 eV when dissociation of the products becomes accessible, according to process (9).

$$M^+ + CS_2 \rightarrow MCS^+ + S \rightarrow M^+ + CS + S \quad (9)$$

For M = Zr and Nb, a third product channel, MC^+, is observed in the reaction of M^+ with CS_2 (reaction (7)). YC^+ was not monitored because it was not detected in the mass scan taken prior to the measurement. The thresholds of $E_0(ZrC^+) = 2.95 \pm 0.14$ eV and $E_0(NbC^+) = 2.59 \pm 0.30$ eV are in reasonable agreement with the thresholds of $E_0(ZrC^+) = 2.79 \pm 0.12$ eV and $E_0(NbC^+) = 2.35 \pm 0.16$ eV calculated using the bond energies given in Tables 1 and 2, verifying that S_2 rather than 2S is the neutral product in reaction (7). The slightly higher experimental thresholds can be rationalized by competition with efficient production of MS^+ and MCS^+. Similar to the MCS^+ cross-sections, MC^+ production also drops sharply near 4.5 eV suggesting formation of MC^+ occurs via a common $SMCS^+$ insertion intermediate.

3.3. Reaction of MS^+ with Xe

MS^+ ions are formed in the flow tube via addition of small amounts of COS to the M^+ beam. Their purity is probed by CID with xenon (reaction (10)). Upon collision with xenon, MS^+ dissociates into M^+ and S (Fig. 2). Analysis of the regularly shaped cross-sections with Eq. (1) yields thresholds of $E_0(M^+) = 6.35 \pm 0.18$ eV, 6.72 ± 0.22, and 6.09 ± 0.16 eV (Tables 3–5), which represent rigorous upper limits [17a,37] to $D_0(M^+–S)$ for M = Y, Zr, and Nb, respectively.

$$MS^+ + Xe \rightarrow M^+ + S + Xe \quad (10)$$

3.4. Reaction of MS^+ with CO

The cross-sections for reaction of MS^+ with CO are depicted in Fig. 3. The three major products, M^+, MO^+, and MOS^+, are formed and attributed to reactions (11)–(14). Inefficient MC^+ ion formation (not shown) is detected at higher energies for M = Nb with a maximum cross-section of $\sigma_{max} = 0.46 \times 10^{-16}$ cm^2 and is attributed to reaction (15). For M = Y and Zr, the MC^+ channel was not monitored because it was not observed in the mass scans routinely performed prior to threshold measurements.

$$MS^+ + CO \rightarrow M^+ + COS \quad (11)$$

$$MS^+ + CO \rightarrow MO^+ + CS \quad (12)$$

$$MS^+ + CO \rightarrow M^+ + CO + S \quad (13)$$

$$MS^+ + CO \rightarrow MOS^+ + C \quad (14)$$

$$MS^+ + CO \rightarrow MC^+ + SO \quad (15)$$

At first glance, the reactivity of MS^+ towards CO seems to be similar for all three metals with formations of M^+ and MO^+ competing at low energies and MOS^+ formation commencing at elevated energies. Note the overall cross-section of the YS^+/CO system is one order of magnitude lower than for ZrS^+/CO and NbS^+/CO. This can possibly be rationalized by the closed-shell character of the YS^+ ($^1\Sigma^+$) species compared to the open shell ZrS^+ ($^2\Delta$) and NbS^+ ($^3\Sigma^-$) molecules (see below), longer Y^+–S bond (2.241 Å versus 2.174 and 2.125 Å), and/or the lower electronegativity calculated according to Mulliken [38] (2.97 eV versus 3.32 and 3.28 eV) of the YS^+ ion. For M = Y and Zr, formation of the metal-oxide cations prevails over the M^+ product at higher energies, whereas for M = Nb, the dissociation into M^+ and S dominates. Closer inspection reveals that several product channels have composite cross-sections most apparent in the M^+ channel. The Y^+ cross-section starts near 3 eV and rises more rapidly above 6.5 eV. Zr^+ formation also sets in near 3 eV and experiences a slope change near 6.5 eV. Formation of Nb^+ begins at a much higher apparent threshold of ~5.5 eV. High-energy formation of M^+ can be attributed to simple CID (reaction (13)) with CO as the collision gas [27a]. However, the cross-sections for Y^+ and Zr^+ clearly extend below the bond energies $D_0(Y^+–S) = 5.49 \pm 0.18$ eV and $D_0(Zr^+–S) = 5.69 \pm 0.10$ eV as indicated by arrows in Fig. 3. Thus, low-energy processes contribute to the Y^+ and Zr^+ channels and can be attributed to reaction (11). It is likely that a similar process also contributes to the Nb^+ threshold; however, the cross-section below 5.5 eV is very small and difficult to fit with Eq. (1). If the low-energy feature for M = Y and Zr is modeled using Eq. (1), the thresholds (Tables 3 and 4) can be converted to $D_0(Y^+–S) = 5.52 \pm 0.17$ eV and $D_0(Zr^+–S) = 5.86 \pm 0.25$ eV. If the model for reaction (11) is subtracted from the M^+ cross-section data, the residual CID cross-section can be modeled leading to thresholds of $E_0(Y^+) = 7.14 \pm 0.14$ eV, $E_0(Zr^+) = 6.93 \pm 0.33$ eV, and $E_0(Nb^+) = 6.09 \pm 0.16$ eV. These Y^+ and Zr^+ thresholds exceed those from CID with Xe, which is in good agreement with the behavior seen in earlier CID studies of MS^+ with CO [27]. In contrast, the threshold obtained from fitting of the Nb^+ channel is very similar to the CID threshold with xenon, which may be because there are contributions from reaction (11) at low energies.

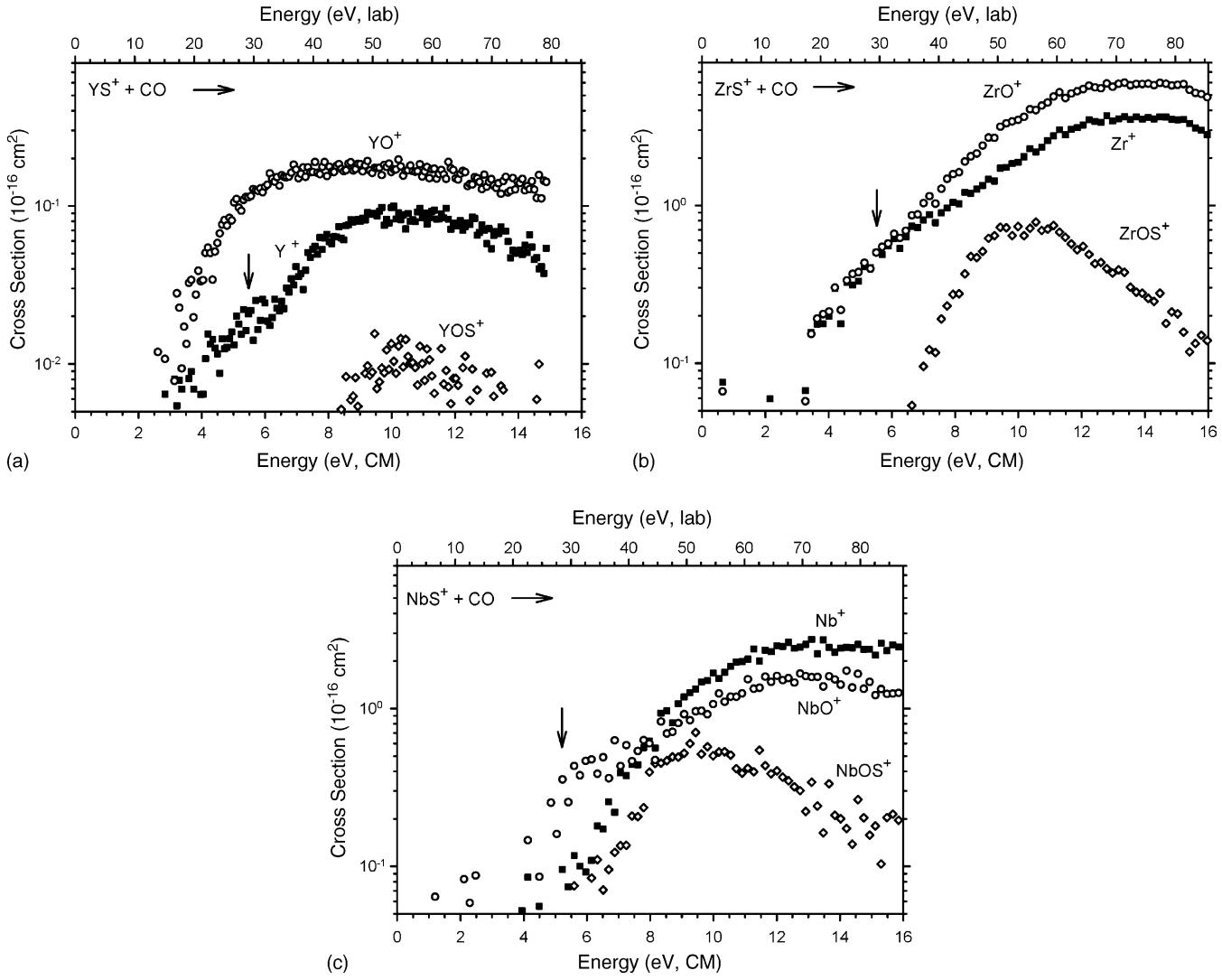

Fig. 3. Product cross-sections for the reaction of MS^+ ((a) YS^+; (b) ZrS^+; (c) NbS^+) with CO to form M^+ (■), MO^+ (◯), and MOS^+ (◊) as a function of center of mass energy (lower axis) and laboratory energy (upper axis). The arrows mark the dissociation energies of YS^+, ZrS^+, and NbS^+ at 5.49, 5.69, and 5.20 eV, respectively. Note that the scale for M = Y is one order of magnitude lower than for the other metals.

The second product formed in the reaction of MS^+ with CO is MO^+ according to process (12). Fitting of the cross-sections with Eq. (1) yields thresholds (Tables 3–5) that can be combined with $D_0(MO^+)$, $D_0(CS)$, and $D_0(CO)$ (Tables 1 and 2) to yield $D_0(Y^+–S) = 6.56 \pm 0.28$ eV, $D_0(Zr^+–S) = 6.57 \pm 0.27$ eV, and $D_0(Nb^+–S) = 5.97 \pm 0.43$ eV. All these bond energies are comparable to the upper limits obtained from CID with Xe, which may suggest the presence of barriers en route to MO^+ formation, as found for the analogous reactions for M = Sc, Ti, and V [27].

Formation of MOS^+ is observed at high energies for all three metals in the MS^+/CO system and can be attributed to oxygen-atom transfer. Analysis of the cross-sections with Eq. (1) results in thresholds (Tables 3–5) that are converted into bond energies using Tables 1 and 2: $D_0(SY^+–O) = 4.14 \pm 0.22$ eV, $D_0(SZr^+–O) = 4.68 \pm 0.24$ eV, and $D_0(SNb^+–O) = 5.56 \pm 0.42$ eV. The MOS^+ cross-sections fall of sharply above 11.109 eV = D_0(CO), where dissociation to $MS^+ + O + C$ becomes accessible.

3.5. Reaction of MS^+ with CO_2

M^+, MO^+, and MOS^+ are the three major product channels observed in the reaction of MS^+ with CO_2 as depicted in Fig. 4. These can be attributed to reactions (16)–(19).

$$MS^+ + CO_2 \rightarrow MO^+ + COS \quad (16)$$

$$MS^+ + CO_2 \rightarrow MOS^+ + CO \quad (17)$$

$$MS^+ + CO_2 \rightarrow MO^+ + CO + S \quad (18)$$

$$MS^+ + CO_2 \rightarrow M^+ + S + CO_2 \quad (19)$$

Comparison of the MS^+/CO_2 cross-sections with those of the MS^+/CO system reveals that now formation of MO^+ and MOS^+ dominates over M^+ formation in the energy range observed. This observation is consistent with the higher number of C–O bonds and the lower C–O bond energy in CO_2, $D_0(OC–O) = 5.453 \pm 0.002$ eV versus $D_0(C–O) = 11.109 \pm 0.005$ eV (Table 2). Note again the sig-

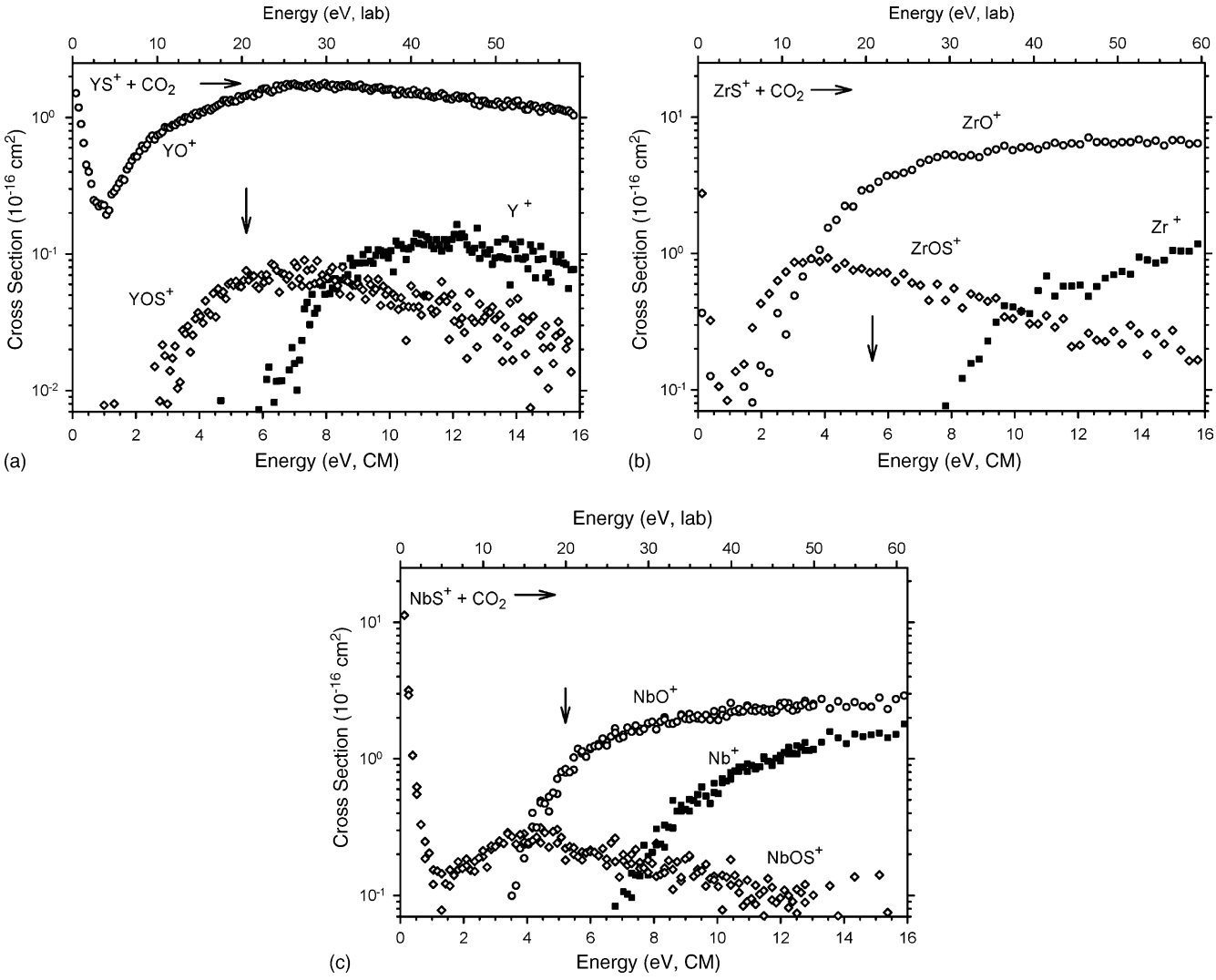

Fig. 4. Product cross-sections for the reaction of MS^+ ((a) YS^+; (b) ZrS^+; (c) NbS^+) with CO_2 to form MO^+ (◯), MOS^+ (◊), and M^+ (■), and as a function of center of mass energy (lower axis) and laboratory energy (upper axis). The arrows mark the dissociation energies of YS^+, ZrS^+, and NbS^+ at 5.49, 5.69, and 5.20 eV, respectively. Note that the scale for M = Y is one order of magnitude lower than for the other metals.

nificantly lower cross-sections for YS^+/CO_2 compared to those for the ZrS^+/CO_2 and NbS^+/CO_2 systems. The YO^+ cross-section consists of a pronounced exothermic, low-energy feature ($\sigma(YO^+) = 2 \times 10^{-16}$ cm^2 at $E_{cm} \approx 0.03$ eV) and an endothermic feature. ZrO^+ exhibits only a very small exothermic tail ($\sigma(ZrO^+) = 0.5 \times 10^{-16}$ cm^2 at $E_{cm} \approx 0.03$ eV) and a pronounced endothermic feature, whereas NbO^+ exhibits only an endothermic cross-section. If the exothermic features for M = Y and Zr are modeled using a power law and subtracted from the MO^+ cross-sections, analysis of the residual cross-sections with Eq. (1) results in $E_0(YO^+) = 1.03 \pm 0.11$ eV, $E_0(ZrO^+) = 1.34 \pm 0.37$ eV, and $E_0(NbO^+) = 3.71 \pm 0.19$ eV. This large difference in thresholds suggests that MO^+ formation occurs via process (16) for reaction of YS^+ and ZrS^+, whereas process (18) can be assigned for reaction of NbS^+. These assignments lead to bond energies of $D_0(Y^+–S) = 6.00 \pm 0.21$ eV, $D_0(Zr^+–S) = 6.79 \pm 0.39$ eV, and $D_0(Nb^+–S) = 5.39 \pm 0.22$ eV. Clearly, contributions to the YO^+ and ZrO^+ cross-sections from reaction (18) are likely at higher energies and this could influence the interpretation of the data. Comparable composite cross-sections have been observed in the MS^+/CO_2 systems with M = Sc, Ti, and V [27].

The question remaining concerns the assignment of the exothermic feature in the YO^+ cross-section. Notably, the YO^+ cross-section in Fig. 4a is the only MO^+ cross-section of the early transition metals (M = Sc, Ti, V, Y, Zr, and Nb) that exhibits a pronounced exothermic feature ($\sigma_0 = 2 \times 10^{-16}$ cm^2 at $E_{cm} = 0.03$ eV). In general, there are four possible origins for the exothermic YO^+ feature. The exothermic behavior could result from: (i) products formed by the reaction of the interfering $(COS)_2^+$ dimer (see above) with CO_2, e.g., the van der Waals complex $(COS\cdots CO_2)^+$, (ii) the presence of excited YS^+ ($^3\Pi$) in the beam, which is predicted to be 2.12 eV above the $^1\Sigma^+$ ground state at the ADF/BP86 level of theory (see below), (iii) the reaction of YS^+ with impurities such as O_2 and H_2O, or (iv) the exothermicity of the reaction of YS^+ with CO_2 to yield YO^+ and COS. Arguments (i) and (ii) can be excluded from further considerations for the following reasons. First, CID with xenon

reveals that the amount of $(COS)_2^+$ dimer in the beam is very low (see above), even though the weak bond in the $(COS)_2^+$ dimer of 0.75 ± 0.04 eV allows efficient bond cleavage [39]. Second, the bond energy of the heterogeneous $(COS\cdots CO_2)^+$ dimer is expected to be lower than that of the symmetric $(COS)_2^+$ dimer. The dissociation energies found for the symmetric dimers are always larger than those of the corresponding heterogeneous dimers [40]. For example: $D_0[(COS)_2^+] = 0.75 \pm 0.04$ eV [39], $D_0[(CS_2)_2^+] = 0.76 \pm 0.04$ eV [41], and $D_0[(COS\cdots CS_2)^+] = 0.25 \pm 0.04$ eV. This would result in an endothermic cross-section for the replacement of COS by CO_2. The presence of large amounts of excited YS^+ ions in the beam is unlikely, because not all of the product cross-sections for the YS^+ reactant show evidence for a contribution from such excited states.

After exclusion of (i) and (ii), the validity of (iii) and (iv) can be probed with FTICR. In order to probe the occurrence of (iii) reactions (20) and (21) are measured with FTICR.

$$YS^+ + O_2 \rightarrow YO^+ + SO \quad (20)$$

$$YS^+ + H_2O \rightarrow YO^+ + H_2S \quad (21)$$

From the pseudo-first order kinetics of reactions (20) and (21) rate constants of $k_{FTICR,(20)} = (4.2 \pm 1.4)$ eV $\times 10^{-10}$ cm^3 s^{-1} molecule^{-1} and $k_{FTICR,(21)} = (5.6 \pm 1.1) \times 10^{-10}$ cm^3 s^{-1} molecule^{-1} are obtained. Comparison of these rate constants with the collision rates $k_c = 5.87 \times 10^{-10}$ and 23.27×10^{-10} cm^3 s^{-1} molecule^{-1} for O_2 and H_2O, respectively, gives efficiencies of $\phi_{O_2}(YO^+) = 0.72 \pm 0.23$ and $\phi_{H_2O}(YO^+) = 0.24 \pm 0.05$. Thus, both reactions may occur when as little as 1% O_2 or H_2O are present in the GIB cell, resulting in an exothermic feature in the YO^+ cross-section.

Next, reaction (22) is probed with FTICR. The observed reactivity corresponds to a rate constant of $k_{FTICR,(22)} = (0.73 \pm 0.25) \times 10^{-10}$ cm^3 s^{-1} molecule^{-1}. However, correction of this rate constant for the presence of ca. 10% O_2 and 40% H_2O in the background of the instrument ($p_{back} = 2.0 \times 10^{-7}$ Pa), using the rate constants of reactions (20) and (21) given above, reduces $k_{FTICR,(22)}$ to virtually zero.

$$YS^+ + CO_2 \rightarrow YO^+ + COS \quad (22)$$

$$YO^+ + COS \rightarrow YS^+ + CO_2 \quad (23)$$

When YO^+ ions are trapped with COS in the FTICR, YS^+ is observed as the major primary product (process (23)). The pseudo-first order kinetics at short reaction times yield a rate constant of $k_{FTICR,(23)} = (0.88 \pm 0.17) \times 10^{-10}$ cm^3 s^{-1} molecule^{-1} and efficiency of $\phi_{COS}(YS^+) = 0.08 \pm 0.02$. (Measurements at $p_{COS} = 0.98$, 2.85, and 7.25×10^{-6} Pa yielded $k_{FTICR,(23)} = 0.95$, 0.82, and 0.87×10^{-10} cm^3 s^{-1} molecule^{-1}, respectively.) At longer reaction times, the kinetics of reaction (23) are obscured by two processes. On the one hand, YO^+ ions are regenerated by reaction of the YS^+ ions with water and oxygen present in the FTICR background (see above). On the other hand, YO^+ ions are depleted by the reaction with background water to yield $YO_2H_2^+$. Both factors render the completion of reaction (23) impossible. Thus, it remains uncertain whether the observed reactivity of YO^+ towards COS stems from ground-state or excited YO^+ ions (see below). The reaction rates for $k_{FTICR,(22)}$ and $k_{FTICR,(23)}$ yield $K_{eq} = 0.83 \pm 0.33$ and hence $\Delta_R G(298\,K) = 0.005 \pm 0.002$ eV upon application of the Gibbs–Helmholtz equation, $\Delta_R G(298\,K) = -RT \ln K_{eq}$. Considering $\Delta\Delta_R G(298\,K/0\,K) = 0.013 \pm 0.001$ eV derived from calculations at the B3LYP/3-21G level of theory, we arrive at $\Delta_R H_0 = 0.018 \pm 0.002$ eV [36]. This $\Delta_R H_0$ value yields $D_0(Y^+–S) = 5.22 \pm 0.16$ eV. Because of the background reactions with H_2O and O_2, the rate constant for process (22) is an upper limit, and the D_0 value is thus a lower limit, in agreement with the bond energy of $D_0(Y^+–S) = 5.49 \pm 0.18$ eV (Table 1).

In the GIB experiments, oxygen-atom transfer leading to MOS^+ formation is observed in the reaction of MS^+ with CO_2. The YOS^+ cross-section has an apparent threshold near 2 eV and starts to level off near 5.5 eV when dissociation of CO_2 into CO and O becomes accessible (Table 2). Fitting of the cross-section results in $E_0(YOS^+) = 1.77 \pm 0.24$ eV and $D_0(SY^+–O) = 3.68 \pm 0.24$ eV. Formation of $ZrOS^+$ exhibits a small exothermic tail ($\sigma(ZrOS^+) = 4 \times 10^{-16}$ cm^2 at $E_{cm} \approx 0.03$ eV) and starts to rise near 1 eV. It is possible that the exothermic tail can be attributed to reaction of ZrS^+ with residual H_2O ($D_0(H_2–O) = 5.034 \pm 0.001$ eV) and/or O_2 ($D_0(O–O) = 5.116 \pm 0.001$ eV), which would suggest that $D_0(SZr^+–O) > 5.0$ eV. Subtraction of the exothermic feature and application of Eq. (1) yields $E_0(ZrOS^+) = 1.07 \pm 0.10$ eV, which is converted to $D_0(SZr^+–O) = 4.38 \pm 0.10$ eV using the values in Tables 1 and 2. This is most conservatively viewed as a lower limit because of the subtraction necessary to evaluate this feature. For M = Nb, the $NbOS^+$ cross-section has a pronounced exothermic feature, $\sigma(NbOS^+) = 54 \times 10^{-16}$ cm^2, which leads to a lower limit of $D_0(SNb^+–O) > 5.453 \pm 0.002$ eV $= D_0(O–CO)$. The value is in good agreement with $D_0(SNb^+–O)$ derived from the NbS^+/CO reaction system, but decreases the range of uncertainty as discussed below.

The least efficient process observed in the MS^+/CO_2 system corresponds to the generation of M^+. The M^+ channel is attributed to CID with CO_2 as collision gas. Eq. (1) yields thresholds of $E_0(Y^+) = 6.43 \pm 0.23$ eV, $E_0(Zr^+) = 6.68 \pm 0.22$ eV, and $E_0(Nb^+) = 6.44 \pm 0.29$ eV. All three thresholds are within experimental error of those obtained for CID with Xe (Tables 3–5).

3.6. Reaction of MS^+ with COS

The reaction of MS^+ with COS leads to exothermic formation of MS_2^+ as the predominant product at low energies (Fig. 5). Endothermic formation of M^+ and MO^+ is observed at higher energies, and inefficient formation of MOS^+ is detected for M = Zr and Nb at high energies with maximum cross-sections $\sigma_{max} < 0.25 \times 10^{-16}$ cm^2 (not shown).

$$MS^+ + COS \rightarrow MS_2^+ + CO \quad (24)$$

$$MS^+ + COS \rightarrow MO^+ + CS_2 \quad (25)$$

$$MS^+ + COS \rightarrow M^+ + S_2 + CO \quad (26)$$

$$MS^+ + COS \rightarrow MO^+ + CS + S \quad (27)$$

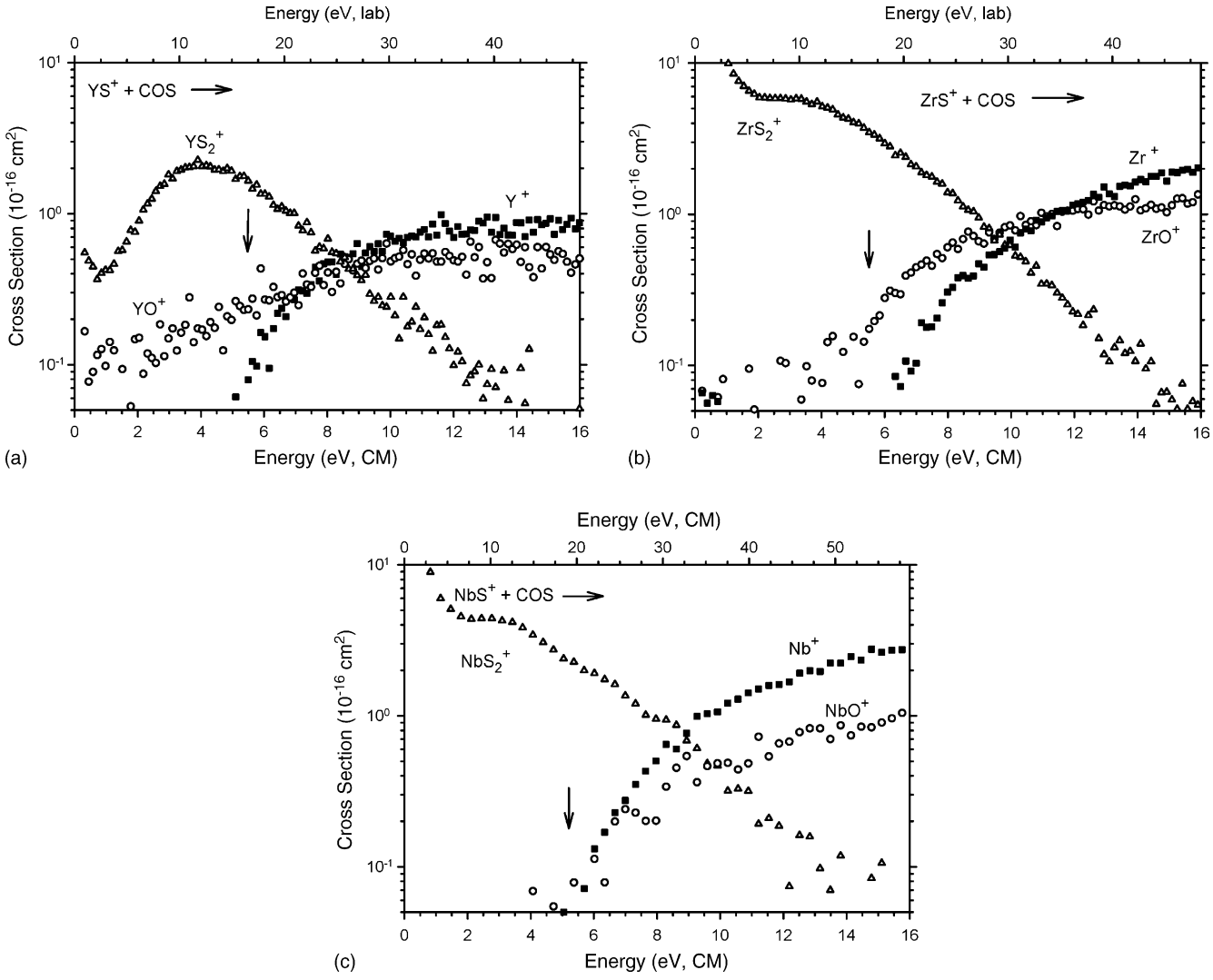

Fig. 5. Product cross-sections for the reaction of MS^+ ((a) YS^+; (b) ZrS^+; (c) NbS^+) with COS to form $MS_2{}^+$ (△), M^+ (■), and MO^+ (◯) as a function of center of mass energy (lower axis) and laboratory energy (upper axis). The arrows mark the dissociation energies of YS^+, ZrS^+, and NbS^+ at 5.49, 5.69, and 5.20 eV, respectively.

The cross-sections for $MS_2{}^+$ formation (reaction (24)) decrease with increasing energy and are therefore exothermic with $\sigma(YS_2{}^+) = 1 \times 10^{-16}\,cm^2$, $\sigma(ZrS_2{}^+) = 188 \times 10^{-16}\,cm^2$, and $\sigma(NbS_2{}^+) = 69 \times 10^{-16}\,cm^2$ at $E_{cm} \sim 0.03$ eV. The exothermic feature is least pronounced for M = Y, as is the case for the isovalent ScS^+/COS system, which can be rationalized by the differences in electronic structure of the MS^+ cations [27a]. Exothermic sulfur transfer from COS implies a lower limit of $D_0(SM^+–S) > 3.140 \pm 0.005$ eV for M = Y, Zr, and Nb. Together with the upper limit of $D_0(SM^+–S) < 4.50 \pm 0.04$ eV derived for M = Y and Zr from failure to observe sequential S-transfer with CS_2 we obtain $D_0(SM^+–S) = 3.84 \pm 0.70$ eV for M = Y and Zr. An endothermic feature is present in all $MS_2{}^+$ cross-sections with a threshold near 1 eV, which may be attributed to formation of $MS_2{}^+$ with a different geometric structure or electronic state as has been observed for other MS^+/COS systems with M = Sc, Ti, and V [27].

The other two products formed according to reactions (25)–(27), MO^+ and M^+, generally have comparable magnitudes, although M^+ prevails at high energies. This is presumably because formation of MO^+ requires breaking the CO bond of $D_0(SC–O) = 6.88 \pm 0.04$ eV, which is stronger in COS compared with CO_2. The MO^+ cross-sections start at apparent thresholds of about 1, 3, and 5 eV for M = Y, Zr, and Nb, respectively. Analysis of the YO^+ cross-section is difficult because of its low intensity and very slow rise. Application of Eq. (1) to the ZrO^+ and NbO^+ channels yields $E_0(ZrO^+) = 1.34 \pm 0.21$ eV and $E_0(NbO^+) = 5.18 \pm 0.52$ eV. The very different thresholds indicate that the ZrO^+ cross-section must be attributed to reaction (25), where the threshold yields $D_0(Zr^+–S) = 6.72 \pm 0.24$ eV, whereas process (27) is assigned to $E_0(NbO^+) = 5.18 \pm 0.52$ eV, leading to $D_0(Nb^+–S) = 5.43 \pm 0.53$ eV. In analogy to the TiS^+/COS system [27a], process (27) is likely to contribute to the ZrO^+ intensity above about 5 eV. Subtraction of the cross-section for process (25) with the parameters given in Table 4 leads to a cross-section for process (27) with $E_0(ZrO^+) = 5.65 \pm 0.34$ eV, which leads to $D_0(Zr^+–S) = 6.53 \pm 0.36$ eV. This value must be viewed cautiously because the subtraction of the low

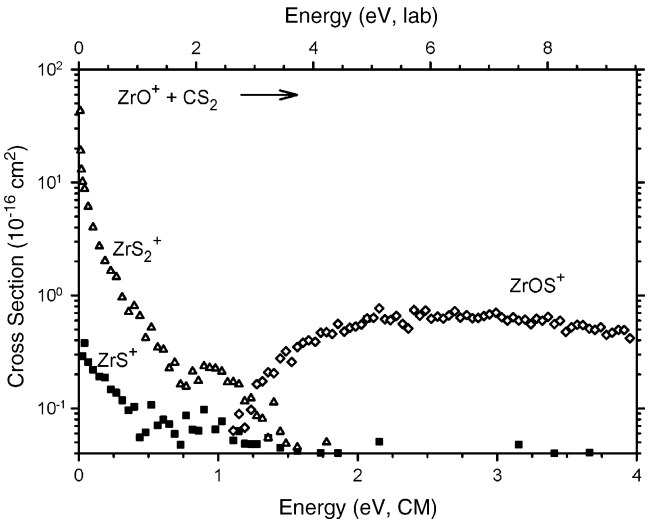

Fig. 6. Product cross-sections for the reaction of ZrO^+ with CS_2 to form $ZrS_2{}^+$ (△), $ZrOS^+$ (◊), and ZrS^+ (■) as a function of center of mass energy (lower axis) and laboratory energy (upper axis).

energy feature assumes that the high energy behavior is known.

Analysis of the M^+ cross-sections with Eq. (1) results in thresholds of $E_0(Y^+) = 4.37 \pm 0.13$ eV, $E_0(Zr^+) = 5.25 \pm 0.16$ eV, and $E_0(Nb^+) = 4.74 \pm 0.33$ eV, clearly below the corresponding thresholds from CID with Xe. This indicates reaction (26) is the source for the M^+ formation at threshold, as also observed for MS^+/COS with M = Sc, Ti, and V [27]. Using process (26) and the thermochemical data in Tables 1 and 2, the thresholds are converted to $D_0(Y^+–S) = 5.59 \pm 0.13$ eV, $D_0(Zr^+–S) = 6.47 \pm 0.13$ eV, and $D_0(Nb^+–S) = 5.96 \pm 0.33$ eV. The formation of M^+ via direct CID with COS as the collision gas, yielding COS + S neutral products, is likely to contribute to the M^+ cross-sections at elevated energies.

3.7. Reaction of MO^+ with CS_2 (M = Zr and Nb)

Reaction of ZrO^+ ions with CS_2 in the GIB results in formation of $ZrS_2{}^+$, ZrS^+, and $ZrOS^+$ (Fig. 6), which are attributed to reactions (28)–(30).

$$ZrO^+ + CS_2 \rightarrow ZrS_2{}^+ + CO \quad (28)$$

$$ZrO^+ + CS_2 \rightarrow ZrS^+ + COS \quad (29)$$

$$ZrO^+ + CS_2 \rightarrow ZrOS^+ + CS \quad (30)$$

Formation of $ZrS_2{}^+$ (reaction (28)) is exothermic with $\sigma(ZrS_2{}^+) = (10 \pm 2) \times 10^{-16}$ cm^2 at 0.03 eV ($k_{GIB}/k_c = 3.3 \pm 0.7\%$) and leads to a lower limit of $D_0(SZr^+–S) > 2.95 \pm 0.17$ eV in good agreement with $D_0(SZr^+–S) > 3.140 \pm 0.005$ eV derived from $ZrS_2{}^+$ formation in the ZrS^+/COS system. The exothermic cross-section for the ZrS^+ channel, $\sigma(ZrS^+) = 0.3 \times 10^{-16}$ cm^2 at 0.03 eV, increases the lower limit of $D_0(Zr^+–S) > 4.50 \pm 0.04$ eV to a lower limit of $D_0(Zr^+–S) > 5.38 \pm 0.12$ eV. The only endothermic process observed is formation of $ZrOS^+$ (process (30)). Analysis of the threshold with Eq. (1) yields $E_0(ZrOS^+) = 1.19 \pm 0.13$ eV, which results in $D_0(OZr^+–S) = 3.31 \pm 0.14$ eV.

In order to further probe the formation of ZrS^+ according to reaction (29), ZrO^+ ions were trapped with CS_2 in the FTICR cell. However, formation of $ZrS_2{}^+$ according to reaction (28) is the only primary product formed with an efficiency of $\phi(MS_2{}^+) = 5 \pm 1\%$, in agreement with the GIB efficiency. ZrO_2H^+ and $ZrSOH^+$ are observed as minor products formed by reaction with background water. Double resonance on ZrS^+ ($m/z = 125$) did not affect the formation of $ZrS_2{}^+$. Thus, ZrS^+ can be excluded as an intermediate in reaction (28). The failure to detect ZrS^+ in the FTICR experiments can be attributed to the very low efficiency ($k_{GIB}/k_c = 0.1\%$) of reaction (29) and the rapid reaction with residual water (see below).

Reaction of NbO^+ with CS_2 was studied with FTICR. The major product channels observed are $NbOS^+$ (15%) and $NbS_2{}^+$ (85%) with reaction efficiencies of $\phi(NbS_2{}^+) = 0.29$ and $\phi(NbOS^+) = 0.06$. No NbS^+ is observed, which may be attributed to slow product formation (as is seen for M = Zr) as well as efficient reaction of NbS^+ with residual water and O_2 to $NbSO^+$ (see below). Double resonance experiments on NbS^+ and $NbOS^+$ reveal that neither of them is a precursor for $NbS_2{}^+$ formation. Direct formation of $NbS_2{}^+$ via process (28) with M = Nb yields a lower limit for $D_0(SNb^+–S) > 2.71 \pm 0.15$ eV (Tables 1 and 2). Observing exothermic formation of $NbOS^+$ implies a lower limit for $D_0(ONb^+–S) > 4.50 \pm 0.04$ eV = D_0(S–CS) (Table 2).

3.8. Reaction of MX^+ with H_2Y (X = O and S; Y = S and O)

In order to independently determine $D_0(M^+–S)$ for M = Y, Zr, and Nb, equilibrium measurements [42] of reaction (2) and its reverse (2′) were attempted in the FTICR. However, the establishment of equilibrium for reaction (2) is rendered difficult because of the efficient reaction with H_2O and O_2 present in the background of the instrument (see above). Therefore, the kinetic approach is employed for an indirect determination of the equilibrium constant K_{eq} [43]. This method involves the separate determination of the rate constants k_2 and $k_{2'}$, along with $K_{eq} = k_2/k_{2'}$. ^{18}O-labeled water is used as the reagent for reaction (2), in order to reduce the perturbation of the kinetics by background H_2O and O_2. Product distributions and reaction rates are summarized in Table 6.

The reaction rates obtained from the pseudo-first order kinetics for M = Y (Table 6) yield $K_{eq} = 108 \pm 43$ [42,44], and hence $\Delta_R G_{298} = -0.12 \pm 0.01$ eV. Applying $\Delta\Delta_R G(298\,K/0\,K) = 0.017 \pm 0.001$ eV derived from calculations at the B3LYP/3-21G level of theory [36], we arrive at $\Delta_R H_0 = -0.10 \pm 0.01$ eV. This value is in reasonable agreement with the $\Delta_R H_0 = -0.28$ eV predicted by calculations of the YS^+/H_2O system at the MP4 level of theory [45]. The experimental $\Delta_R H_0$ yields $D_0(Y^+–S) = 5.28 \pm 0.18$ eV, which is within the error margins of $D_0(Y^+–S) = 5.52 \pm 0.17$ and 5.59 ± 0.13 eV (Table 3) obtained from the thresholds of reactions (11) and (26).

MO^+ formation according to process (2) is observed with a branching ratio of 80% in the FTICR for M = Zr

Table 6
Product distributions, rate constants k_{MX^+} (X = O and S)[a] and reaction enthalpies $\Delta_R H_0$ for reaction with H_2O and H_2S for M = Y, Zr, and Nb

MX	Reaction	MO^+ (%)	MOS^+ (%)	$MOSH^+$ (%)	k_{MO^+}	$\phi(MO^+)$[b]	$\Delta_R H_0$ (eV)[c]
YS^+	(2)/(21)	100[d]	–	–	5.6	0.24	-0.10 ± 0.01
ZrS^+	(2)	80	–	20	4.8	0.20	$<-0.15 \pm 0.01$
NbS^+	(2)	15	85	–	0.36	0.02	0.013 ± 0.055
		MS^+ (%)	MOS^+ (%)	$MOSH^+$ (%)	k_{MS^+}	$\phi(MS^+)$	
YO^+	(2′)	100	–	–	0.052	0.004	
ZrO^+	(2′)	<10[e]	–	100	<0.007	<0.0005	
NbO^+	(2′)	10	90	–	0.25	0.02	

[a] Rate constants k are given in 10^{-10} cm^3 s^{-1} molecules^{-1}.
[b] Reaction efficiency $\phi(MX^+) = k_{exp}/k_c$.
[c] $\Delta_R H_0$ is derived using $\Delta_R G_{298} = -RT \ln K_{eq}$ and $\Delta\Delta_R G(298\,K/0\,K) = 0.017 \pm 0.001$ eV obtained at the B3LYP/3-21G level of theory.
[d] Adduct formation, $YS(H_2O)^+$, is observed with 10%.
[e] ZrS^+ formation is *not* observed, the value given here is derived from the S/N ratio observed after trapping of ZrO^+ for 5 s in $p_{H_2S} = 1.3 \times 10^{-5}$ Pa.

with a reaction rate of $k_2 = 4.8 \times 10^{-10}$ cm^3 s^{-1} molecule^{-1}. However the reverse reaction (process (2′)) is not observed because of pronounced formation of $ZrOSH^+$ (100%). Using the signal-to-noise ratio of the FTICR spectrum, we determine an upper limit for ZrS^+ production of 10% in process (2′), which leads to an upper limit for $k_{2'} < 0.007 \times 10^{-10}$ cm^3 s^{-1} molecule^{-1}. Combination of k_2 and $k_{2'}$ leads to an upper limit of $\Delta_R H_0 < -0.15 \pm 0.01$ eV resulting in $D_0(Zr^+–S) < 5.66 \pm 0.11$ eV. Formation of NbO^+ and NbS^+ in processes (2) and (2′) with M = Nb is observed in the FTICR (Table 6), but the dominant product channel in both cases is formation of $NbOS^+$. Observation of the latter in exothermic reactions leads to lower limits of $D_0(SNb^+–O) > 5.034 \pm 0.001$ eV and $D_0(ONb^+–S) > 3.029 \pm 0.009$ eV in good agreement with $D_0(SNb^+–O) = 5.56 \pm 0.42$ eV determined from threshold analysis of process (14). Using the reaction rates obtained for NbO^+ and NbS^+ formation (Table 6), we derive $K_{eq} = 1.4 \pm 0.4$ and hence $\Delta_R H_0 = 0.008 \pm 0.003$ eV and $D_0(Nb^+–S) = 5.13 \pm 0.11$ eV. At this point, a note of caution about this approach to equilibrium thermochemistry is indicated because the efficiently competing formation of $NbOS^+$ may influence the reaction rates. If this competing reaction occurs with a comparable rate for both directions in reaction (2), the indirect approach used above results in values close to the true thermochemical equilibrium. In the other extreme, however, one component may undergo the competing reaction much more rapidly than the other, which would still lead to a quasi-stationary state, but not to a true equilibrium. As a conservative error estimation, the resulting extremes might be considered accordingly. Using the data given in Table 6 as the extremes, K_{eq} could vary between 0.14 and 10 for reaction (2) with M = Nb, leading to $\Delta_R H(0\,K) = 0.013 \pm 0.055$ eV, and hence $D_0(Nb^+–S) = 5.13 \pm 0.12$ eV is the final value derived from the FTICR measurements.

4. Theoretical results

To fully understand the experimental results, it is important to know the nature of the electronic states of the MS^+ species. DFT calculations were used to provide this information. At the ADF/BP level of theory (Table 7), we find low-spin $^1\Sigma^+$, $^2\Delta$, and $^3\Sigma^-$ ground states for YS^+, ZrS^+, and NbS^+, respectively. These states result from the perfect pairing of Y^+ (^{1}S), Zr^+ (^{4}F), and Nb^+ (^{5}D) [46] with S (^{3}P) [32] yielding $(1\sigma)^2(2\sigma)^2(1\pi)^4$, $(1\sigma)^2(2\sigma)^2(1\pi)^4(1\delta)^1$, and $(1\sigma)^2(2\sigma)^2(1\pi)^4(1\delta)^2$ valence configurations, respectively. The $^1\Sigma^+$ ground state for yttrium sulfide agrees with calculations at the B3LYP level of theory [47]. The next higher states of YS^+ are the three triplet states at 2.12, 2.58, and 2.66 eV with $^3\Pi$, $^3\Pi/^3\Phi$, and $^3\Sigma^+$ symmetry formed by excitation of a single electron from the 1π orbital into the 3σ ($^3\Pi$) or 1δ orbital ($^3\Pi/^3\Phi$) or from the 2σ into the 3σ orbital ($^3\Sigma^+$). The two lowest quintet states, $^5\Delta$ and $^5\Sigma^+$, of YS^+ have $(1\sigma)^2(2\sigma)^2(1\pi)^2(1\delta)^1(3\sigma)^1$ and $(1\sigma)^2(2\sigma)^2(1\pi)^2(1\delta)^2$ configurations and are located at 4.88 and 5.83 eV, respectively. Not surprisingly, the splitting between the ground state and the lowest excited state is much narrower for ZrS^+ and NbS^+, which both have electrons in the non-bonding δ-manifold. The lowest excited state is ZrS^+ ($^2\Sigma^+$) at 0.30 eV followed by a ($^2\Pi$) state at 1.28 eV. The $^2\Sigma^+$ state is reached via excitation of the uncoupled electron from the 1δ to the 3σ orbital, whereas the $^2\Pi$ state is accessed via excitation of the electron from the 1δ orbital into an unoccupied 2π orbital. The lowest quartet states are formed by excitation of one electron from one of the doubly occupied 1π orbitals into either the empty 3σ or 1δ orbitals requiring 2.14 eV ($^4\Pi/^4\Phi$) and 2.26 eV ($^4\Pi$), respectively. For NbS^+, the lowest excited state is ($^3\Delta$) at 0.64 eV followed by a ($^3\Pi/^3\Phi$) state at 1.44 eV. The $^3\Delta$ involves excitation of an electron from an occupied 1δ orbital to the 3σ orbital, whereas the $^3\Pi$ state is accessed via excitation of an electron from a singly occupied 1δ orbital into an empty 2π orbital. The lowest quintet states ($^5\Pi$ and $^5\Delta/\Sigma$ symmetry) are formed by excitation of one electron from one of the doubly occupied 1π orbitals into either the 3σ orbital or an empty 2π orbital requiring 2.25 and 2.53 eV, respectively. We choose not to report theoretical bond energies because the ADF program used is not designed to assess accurate bond energies.

5. Discussion

The discussion serves to evaluate and combine the values for $D_0(M^+–S)$, $D_0(M^+–CS)$, $\Delta_f H_0(MOS^+)$, and $\Delta_f H_0(MS_2^+)$

Table 7
State splittings in eV and bond lengths r in Å for MS^+ (M = Y, Zr, and Nb) at the ADF/BP86 level of theory

YS^+			ZrS^+			NbS^+		
E_{rel}	State	r	E_{rel}	State	r	E_{rel}	State	r
0.00	$^1\Sigma^+$	2.241[a]	0.00	$^2\Delta$	2.174[b]	0.00	$^3\Sigma^-$	2.125[c]
2.12	$^3\Pi$	2.476	0.30	$^2\Sigma^+$	2.156	0.64	$^3\Delta$	2.117
2.58	$^3\Pi/^3\Phi$[d]	2.439	1.28	$^2\Pi$	2.210	1.44	$^3\Pi/^3\Phi$[d]	2.164
2.66	$^3\Sigma^+$	2.333	2.14	$^4\Pi/^4\Phi$[d]	2.350	2.25	$^5\Pi$	2.295
4.88	$^5\Delta$	2.967	2.26	$^4\Pi$	2.381	2.53	$^5\Delta/\Sigma^+$	2.358
5.83	$^5\Sigma^+$	2.933	2.73	$^4\Delta$	2.432			

[a] Reoptimization at the B3LYP/6-311 + G* level of theory yields r = 2.244 Å and ν = 540 cm^{-1}.
[b] Reoptimization at the B3LYP/6-311 + G* level of theory yields r = 2.196 Å and ν = 547 cm^{-1}.
[c] Reoptimization at the B3LYP/6-311 + G* level of theory yields r = 2.154 Å and ν = 541 cm^{-1}.
[d] A differentiation between Π and Φ states is not possible in the employed ADF/BP86 method.

derived above for M = Y, Zr, and Nb. Reaction of M^+ with COS/CS_2 and CID with Xe result in brackets for $D_0(M^+–S)$. The brackets are then used to evaluate the $D_0(M^+–S)$ values derived via the reactions of MS^+ with CO, CO_2, and COS as well as $MO^+ + CS_2$. $D_0(M^+–S)$ values obtained independently from indirect equilibrium measurements of reaction (2) and its reverse (2′) are compared to the $D_0(M^+–S)$ values from the MS^+/COX systems (X = no atom, O, and S). Subsequently, recommended values for $D_0(M^+–S)$ with M = Y, Zr, and Nb are derived. The $D_0(M^+–S)$ values are reported as weighted averages of several independent measurements, which take into account the proportional relevance (given by the error range reported) of each bond energy value. Finally, $D_0(M^+–CS)$, and $\Delta_f H_0(MOS^+)$ for M = Y, Zr, and Nb are addressed.

5.1. Brackets

Using the exothermic formation of MS^+ in reactions (3) and (5), we assign the lower limits of 3.140 ± 0.005 and 4.50 ± 0.04 eV, respectively, to $D_0(M^+–S)$. CID of MS^+ with xenon (process (10)) results in upper limits of $D_0(Y^+–S) < 6.35 \pm 0.18$ eV, $D_0(Zr^+–S) < 6.72 \pm 0.22$ eV, and $D_0(Nb^+–S) < 6.09 \pm 0.16$ eV. The threshold of CID with CO_2 (process (19)) is comparable to the upper limits within experimental error. Thus, we arrive at the following brackets:

$$4.50 \pm 0.04\,(CS_2) < D_0(Y^+–S) < 6.35 \pm 0.18\,(Xe)$$

$$4.50 \pm 0.04\,(CS_2) < D_0(Zr^+–S) < 6.72 \pm 0.22\,(Xe)$$

$$4.50 \pm 0.04\,(CS_2) < D_0(Nb^+–S) < 6.09 \pm 0.16\,(Xe)$$

Note that CID with strongly bound, small molecules often leads to upper limits [27,36] and therefore bond energies derived from processes (13) and (19) will not be included in the averages determined in the following sections.

5.2. Reactions with oxygen-transferring reagents

As has been observed in other MS^+/COX systems (M = Sc, Ti, and V; X = no atom, O, and S) [27], MO^+ formation appears to be associated with a kinetic barrier resulting in $D_0(M^+–S)$ values exceeding those derived from CID with Xe (Tables 3–5). In our previous work, these barriers were explained by the involvement of a metathesis-like mechanism via a four-centered transition state [27]. A series of recent calculations by Xie et al. [47,48] modify our proposal by predicting the formation of a metastable, four-centered MSCOX complex en route to S/O exchange in the case of M = Y and X = O and S. This complex can decompose by a pair of four-centered transition states that only differ in the length of their YS, YO, CS, and CO bonds (Scheme 1). A similar reaction pathway can be envisioned for M = Zr and Nb.

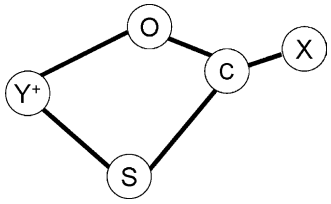

Scheme 1.

Thresholds remaining for refinement of $D_0(M^+–S)$ are those from reactions (11) and (26) for M = Y, (11) for M = Zr, and process (26) for M = Nb. The two values of $D_0(Y^+–S) = 5.52 \pm 0.17$ and 5.59 ± 0.13 eV are consistent with each other and are inside the D_0 bracket given above. Our best GIB value for M = Zr is $D_0(Zr^+–S) = 5.86 \pm 0.25$ eV, which is consistent with the brackets derived above. For M = Zr, the observation of exothermic ZrS^+ formation in the reaction of ZrO^+ and CS_2 (process (29)) leads to a refinement of the lower limit to $D_0(Zr^+–S) > 5.38 \pm 0.12$ eV. For M = Nb, Table 5 shows that $D_0(Nb^+–S) = 5.96 \pm 0.33$ eV derived from process (26) is very close to the upper bracket from CID and is also significantly higher than the D_0 values obtained from processes (18) and (27), $D_0(Nb^+–S) = 5.39 \pm 0.22$ and 5.43 ± 0.53 eV, respectively. A disadvantage of the MS^+/COX systems is that the product cross-sections are often composed of contributions from more than one process and that the characterization of the neutral species formed can be ambiguous.

5.3. $MX^+ + H_2Y$

Indirect equilibrium measurements of MS^+ and MO^+ with H_2O and H_2S yield $D_0(Y^+–S) = 5.28 \pm 0.18$ eV, $D_0(Zr^+–S) < 5.66 \pm 0.11$ eV, and $D_0(Nb^+–S) = 5.13 \pm 0.12$ eV.

Comparison of these three values with $D_0(Y^+–S) = 5.52 \pm 0.17$ eV/5.59 ± 0.13 eV, $D_0(Zr^+–S) = 5.86 \pm 0.25$ eV, and $D_0(Nb^+–S) = 5.39 \pm 0.22$ eV/5.43 ± 0.53 eV shows that the bond energies overlap within their uncertainties for M = Y, Zr, and Nb. A similar observation was made for M = Sc and Ti [27a].

The $D_0(Y^+–S)$ values from reactions (2), (11), and (26), i.e., $D_0(Y^+–S) = 5.28 \pm 0.18$ eV, $D_0(Y^+–S) = 5.52 \pm 0.17$ eV, and $D_0(Y^+–S) = 5.59 \pm 0.13$ eV, yield a weighted average of $D_0(Y^+–S) = 5.49 \pm 0.18$ eV, reported here with two standard deviations of the mean. If we combine the upper limit of $D_0(Zr^+–S) < 5.66 \pm 0.11$ eV obtained from reaction (2) with the bond energy of $D_0(Zr^+–S) = 5.86 \pm 0.25$ eV obtained from reaction (11), we conclude that $D_0(Zr^+–S) = 5.69 \pm 0.10$ eV. Calculation of $D_0(Zr^+–S)$ employing the bond energy of neutral ZrS ($D_0(Zr–S) = 5.92 \pm 0.17$ eV [49]) as well as the ionization energies of neutral ZrS (IE(ZrS) = 7.1 ± 0.7 eV [50]) and neutral Zr (IE(Zr) = 6.634 eV [51]) yields $D_0(Zr^+–S) = 5.54 \pm 0.72$ eV, which is in excellent agreement with $D_0(Zr^+–S) = 5.69 \pm 0.10$ eV. In the case of M = Nb, the weighted statistical average of the values from the MS^+/COX systems and the indirect equilibrium values from the of NbS^+ and NbO^+ with H_2O and H_2S leads to $D_0(Nb^+–S) = 5.20 \pm 0.21$ eV. Thus, we arrive at final values of $D_0(Y^+–S) = 5.49 \pm 0.18$ eV, $D_0(Zr^+–S) = 5.69 \pm 0.10$ eV, and $D_0(Nb^+–S) = 5.20 \pm 0.21$ eV (Table 1).

5.4. Metal thiocarbonyls and oxy sulfides

The reactions of M^+ with CS_2 result in endothermic formation of MCS^+ (process (6)). The observed thresholds (Tables 3–5) are converted to $D_0(Y^+–CS) = 1.42 \pm 0.08$ eV, $D_0(Zr^+–CS) = 2.67 \pm 0.11$ eV, and $D_0(Nb^+–CS) = 2.51 \pm 0.11$ eV using the thermochemical data given in Tables 1 and 2. Assuming reaction (6) occurs via insertion of M^+ into the C–S bond of CS_2, it is likely that the structure of the MCS^+ product can be represented as thiocarbonyl complex. Comparison of $D_0(M^+–CO)$ and $D_0(M^+–CS)$ reveals that the thiocarbonyl ligand binds more strongly than the carbonyl ligand in good agreement with observations made for M = Sc, Ti, and V [27].

Thresholds of processes (14) and (17) lead to $D_0(SY^+–O) = 4.14 \pm 0.22$ and 3.68 ± 0.24 eV, $D_0(SZr^+–O) = 4.68 \pm 0.24$ and 4.38 ± 0.10 eV, and $D_0(SNb^+–O) = 5.56 \pm 0.21$ and $>5.453 \pm 0.005$ eV. Weighted averages (reported with two standard deviations) are calculated as $D_0(SY^+–O) = 3.93 \pm 0.32$ eV and $D_0(SZr^+–O) = 4.42 \pm 0.18$ eV, whereas the lower limit for $D_0(SNb^+–O)$ can be used to reduce the uncertainty of this bond energy to 5.61 ± 0.16 eV. These bond energies can be converted to $\Delta_f H_0(YOS^+) = 6.59 \pm 0.37$ eV, $\Delta_f H_0(ZrOS^+) = 8.45 \pm 0.33$ eV, and $\Delta_f H_0(NbOS^+) = 9.05 \pm 0.27$ eV as well as $D_0(OY^+–S) = 2.14 \pm 0.42$ eV, $D_0(OZr^+–S) = 2.36 \pm 0.44$ eV, and $D_0(ONb^+–S) = 3.68 \pm 0.31$ eV using the thermodynamic data in Tables 1 and 2. Interestingly, process (30) enables direct access to $D_0(OM^+–S)$ for M = Zr and Nb. The threshold of $E_0(ZrOS^+) = 1.19 \pm 0.13$ eV is converted to $D_0(OZr^+–S) = 3.31 \pm 0.14$ eV and $\Delta_f H_0(ZrOS^+) = 7.50 \pm 0.32$ eV using Tables 1 and 2. A lower limit of $D_0(ONb^+–S) > 4.50 \pm 0.04$ eV is obtained for M = Nb. Both values exceed those derived from processes (14) and (17), which may be attributed to the presence of barriers in reactions (14) and (17). Comparison of $D_0(OM^+–S)$ with $D_0(SM^+–S)$ and $D_0(SM^+–S)$ with $D_0(M^+–S)$ (Table 1) shows that the presence of oxygen or a second sulfur ligand results in a lowered M–S bond energy.

6. Summary

The gas-phase reactivities of the early transition-metal sulfide cations YS^+, ZrS^+, and NbS^+ have been investigated with guided-ion beam and Fourier-transform ion-cyclotron resonance mass spectrometry. Careful analysis and evaluation of the threshold energies, reactivities, and cross-sections results in bond dissociation energies of $D_0(Y^+–S) = 5.49 \pm 0.18$ eV, $D_0(Zr^+–S) = 5.69 \pm 0.10$ eV, and $D_0(Nb^+–S) = 5.20 \pm 0.21$ eV. Further, the metal thiocarbonyl binding energies of $D_0(Y^+–CS) = 1.42 \pm 0.08$ eV, $D_0(Zr^+–CS) = 2.67 \pm 0.11$ eV, and $D_0(Nb^+–CS) = 2.51 \pm 0.11$ eV have been obtained. Observation of MOS^+ formation in several of the reactions studied implies $\Delta_f H_0(YOS^+) = 6.59 \pm 0.37$ eV, $\Delta_f H_0(ZrOS^+) = 8.45 \pm 0.33$ eV, and $\Delta_f H_0(NbOS^+) = 9.05 \pm 0.27$ eV.

Acknowledgements

This work was supported by the Deutsche Forschungsgemeinschaft, the Fonds der Chemischen Industrie, the Freunde der Technischen Universität Berlin, and the National Science Foundation (PBA, CHE-0135517, and CHE-041477). In addition, we thank the Konrad-Zuse Institut, Berlin, for the generous allocation of computer time.

References

[1] W. Kai, M.T. Chang, C.D. Liu, T.W. Lee, Oxid. Met. 57 (2002) 523.
[2] S.S. Trond, J.S. Martin, J.P. Stanavage, A.L. Smith, J. Electrochem. Soc. 116 (1969) 1047.
[3] M. Mikami, A. Oshiyama, Phys. Rev. B 57 (1998) 8939.
[4] M. Mikami, A. Oshiyama, Phys. Rev. B 60 (1999) 1707.
[5] B. Liang, L. Andrews, J. Phys. Chem. 106 (2002) 6295.
[6] N. Allali, A. Yacoubi, A. Nadiri, C. Geantet, M. Danot, Ann. Chim. Sci. Mater. 23 (1998) 209.
[7] P. Lavela, J. Morales, L. Sanchez, J.L. Tirado, J. Power Sources 68 (1997) 704.
[8] V. Gaborit, N. Allali, C. Geantet, M. Breysse, M. Virant, M. Danot, Catal. Today 57 (2000) 267.
[9] J. Afonso, M. Breysse, N. Allali, M. Danot, Catal. Today 28 (1996) 23.
[10] W.M.R. Divigalpitiya, R.F. Frindt, S.R. Morrison, J. Phys. D: Appl. Phys. 23 (1990) 966.
[11] S.Y. Istomin, A.Y. Grippa, O.G. D'yachenko, E.V. Antipov, G. Svensson, J.L. Tholence, Physica C 300 (1998) 67.
[12] K.M. Ervin, P.B. Armentrout, J. Chem. Phys. 83 (1985) 166.
[13] R.H. Schultz, P.B. Armentrout, Int. J. Mass Spectrom. Ion Processes 107 (1991) 29.
[14] (a) N. Aristov, P.B. Armentrout, J. Am. Chem. Soc. 106 (1984) 4065; (b) N. Aristov, P.B. Armentrout, J. Am. Chem. Soc. 108 (1986) 1806; (c) N. Aristov, P.B. Armentrout, J. Phys. Chem. 91 (1987) 6178; (d) D.E. Clemmer, L.S. Sunderlin, P.B. Armentrout, J. Phys. Chem. 94 (1990) 208.

[15] (a) P.R. Kemper, M.T. Bowers, J. Phys. Chem. 95 (1991) 5134;
(b) C.L. Haynes, P.B. Armentrout, Organometallics 13 (1994) 3480.
[16] (a) L.S. Sunderlin, P.B. Armentrout, J. Phys. Chem. 92 (1988) 1209;
(b) Y.-M. Chen, D.E. Clemmer, P.B. Armentrout, J. Phys. Chem. 98 (1994) 11490.
[17] (a) R.H. Schultz, K.C. Crellin, P.B. Armentrout, J. Am. Chem. Soc. 113 (1991) 8590;
(b) P.B. Armentrout, in: N.G. Adams, L.M. Babock (Eds.), Advances in Gas Phase Ion Chemistry, vol. 1, JAI Press, Greenwich, 1992, p. 83.
[18] (a) K. Eller, H. Schwarz, Int. J. Mass Spectrom. Ion Processes 93 (1989) 243;
(b) K. Eller, W. Zummack, H. Schwarz, J. Am. Chem. Soc. 112 (1990) 621.
[19] R.A. Forbes, F.H. Laukien, J. Wronka, Int. J. Mass Spectrom. Ion Processes 83 (1988) 23.
[20] (a) T. Su, W.J. Chesnavich, J. Chem. Phys. 76 (1982) 5183;
(b) T. Su, J. Chem. Phys. 88 (1988) 4102;
(c) T. Su, J. Chem. Phys. 89 (1988) 5355.
[21] The ADF Package is available from: G. te Velde, E.J. Baerends, Department of Theoretical Chemistry, Vrije Universiteit, Amsterdam, The Netherlands.
[22] J.G. Snijders, E. Baerends, J. Mol. Phys. 33 (1977) 1651.
[23] S.H. Vosko, L. Wilk, M. Nusair, Can. J. Phys. 58 (1980) 1200.
[24] A.D. Becke, Phys. Rev. A 38 (1988) 3098.
[25] J.P. Perdew, Phys. Rev. B 33 (1986) 8822.
[26] M. Levy, J.P. Perdew, Int. J. Quant. Chem. 49 (1994) 539.
[27] (a) I. Kretzschmar, D. Schröder, H. Schwarz, C. Rue, P.B. Armentrout, J. Phys. Chem. A 104 (2000) 5046;
(b) I. Kretzschmar, D. Schröder, H. Schwarz, C. Rue, P.B. Armentrout, J. Phys. Chem. A 102 (1998) 10060;
(c) I. Kretzschmar, D. Schröder, H. Schwarz, P.B. Armentrout, in: M.A. Duncan (Ed.), Advances in Metal and Semiconductor Clusters—Metal–Ligand Bonding and Metal-Ion Solvation, vol. 5, Elsevier, New York, 2001, p. 347.
[28] G. Gioumousis, D.P. Stevenson, J. Chem. Phys. 29 (1958) 292.
[29] R.H. Schultz, P.B. Armentrout, J. Chem. Phys. 96 (1992) 1036.
[30] P. Tosi, C. Delvai, D. Bassi, O. Dmitriev, D. Cappelletti, F. Vecchiocattivi, Chem. Phys. 209 (1996) 227.
[31] S.G. Lias, J.E. Bartmess, J.F. Liebman, J.L. Holmes, R.D. Levin, W.G. Mallard, J. Chem. Phys. Ref. Data 17 (Suppl. 1) (1988).
[32] C.E. Moore, Atomic Energy Levels, National Standard Reference Data Series, NSRDS-NBS 35, National Bureau of Standards, Washington, DC, 1971.
[33] M.R. Sievers, Y.-M. Chen, P.B. Armentrout, J. Chem. Phys. 105 (1996) 6322.
[34] J.D. Burley, M.K. Ervin, P.B. Armentrout, Int. J. Mass Spectrom. Ion Processes 80 (1987) 153.
[35] K.M. Ervin, P.B. Armentrout, J. Chem. Phys. 83 (1985) 166.
[36] I. Kretzschmar, Ph.D. Thesis, TU Berlin, 1999, D83.
[37] D.A. Hales, L. Lian, P.B. Armentrout, Int. J. Mass Spectrom. Ion Processes 102 (1990) 269.
[38] J.E. Huheey, Inorganic Chemistry: Principles of Structure and Reactivity, third ed., Harper Collins Publishers, New York, 1983, p. 137.
[39] Y. Ono, E.A. Osuch, C.Y. Ng, J. Chem. Phys. 74 (1981) 1645.
[40] (a) C.Y. Ng, D.J. Trevor, B.H. Mahan, Y.T. Lee, J. Chem. Phys. 66 (1977) 446;
(b) C.Y. Ng, P.W. Tiedemann, B.H. Mahan, Y.T. Lee, J. Chem. Phys. 66 (1977) 5737.
[41] Y. Ono, S.H. Linn, H.F. Prest, M.E. Gress, C.Y. Ng, J. Chem. Phys. 73 (1980) 2523.
[42] (a) D. Schröder, J. Hrušák, R. Hertwig, W. Koch, P. Schwerdtfeger, H. Schwarz, Organometallics 14 (1995) 312;
(b) M. Dieterle, J.N. Harvey, D. Schröder, H. Schwarz, C. Heinemann, J. Schwarz, Chem. Phys. Lett. 277 (1997) 399.
[43] J.-Y. Salpin, M. Mormann, J. Tortajada, M.-T. Nguyen, D. Kuck, Eur. J. Mass Spectrom. 9 (2003) 361.
[44] (a) V. Baranov, G. Javahery, A.C. Hopkinson, D.K. Bohme, J. Am. Chem. Soc. 117 (1995) 12801;
(b) G. Bouchoux, J.Y. Salpin, D. Leblanc, Int. J. Mass Spectrom. Ion Processes 153 (1996) 37.
[45] X.-G. Xie, S. Ye, H. Cao, Y.-M. Zhou, N.-H. Shi, THEOCHEM 589–590 (2002) 37.
[46] J. Sugar, C. Corliss, J. Phys. Chem. Ref. Data 14 (Suppl. 2) (1985).
[47] X.-G. Xie, Chem. Phys. 299 (2004) 33.
[48] X.-G. Xie, S. Ye, H. Cao, Y.-M. Zhou, H. Cao, N.-H. Shi, THEOCHEM 618 (2002) 127.
[49] R.P. Steiger, E.D. Drowart, High Temp. Sci. 7 (1975) 288.
[50] L. Karlson, C. Lundevall, J. Phys. B: At. Mol. Opt. Phys. 31 (1998) 491.
[51] P.A. Hackett, M.R. Humphries, S.A. Mitchell, D.M. Rayner, J. Chem. Phys. 85 (1986) 319.
[52] D.D. Wagman, W.H. Evans, V.B. Parker, R.H. Schumm, I. Halow, S.M. Bailey, K.L. Churney, R.L. Nuttall, J. Phys. Ref. Data 11 (Suppl. 2) (1982).
[53] M.W. Chase Jr., C.A. Davies, J.R. Downey Jr., D.J. Frurip, R.A. McDonald, A.N. Syverud, J. Phys. Chem. Ref. Data 14 (Suppl. 1) (1985) (JANAF tables).
[54] M.R. Sievers, P.B. Armentrout, Inorg. Chem. 38 (1999) 397.
[55] M.R. Sievers, P.B. Armentrout, Int. J. Mass Spectrom. 185/187 (1999) 117.
[56] M.R. Sievers, P.B. Armentrout, Int. J. Mass Spectrom. 179/180 (1998) 103.
[57] D.E. Clemmer, N.F. Dalleska, P.B. Armentrout, Chem. Phys. Lett. 190 (1992) 259.
[58] D.A. Prinslow, P.B. Armentrout, J. Chem. Phys. 94 (1991) 3563.
[59] J.B. Pedley, R.D. Naylor, S.P. Kirby, Thermochemical Data of Organic Compounds, Chapman and Hall, London, 1986.